DIBOSON PHYSICS WITH CMS DETECTOR

by

IRAKLI SVINTRADZE

B.S. Tbilisi State University, Republic of Georgia, 2002

AN ABSTRACT OF A DISSERTATION

submitted in partial fulfillment of the
requirements for the degree

DOCTOR OF PHILOSOPHY

Department of Physics
College of Arts and Sciences

KANSAS STATE UNIVERSITY
Manhattan, Kansas
2013

Abstract

In this dissertation, you will find a study of di-boson production in pp collision with the Compact Muon Solenoid (CMS) detector at Large Hadron Collider (LHC). A study of $\mathrm{Z}\gamma \rightarrow \mu\mu\gamma$ process is performed on the data collected by the CMS during 2011 and corresponding to integrated luminosity $\mathcal{L}$= 5 fb^{-1}. The study consists of two parts: cross section measurement and setting the limits on anomalous trilinear gauge couplings (aTGC) between a Z boson and a photon.

The measured cross-section of $\mathrm{Z}\gamma \rightarrow \mu\mu\gamma$ agrees within the uncertainties with the standard model predicted cross section at next to leading order. Having found no excess in cross section measurement, we set the 95% confidence level (C.L.) limit on aTGC, corresponding to: $|h_3^\gamma| < 0.013$, $|h_4^\gamma| < 0.00012$, $|h_3^\mathrm{Z}| < 0.011$ and $|h_4^\mathrm{Z}| < 0.00011$.

Another study discussed is a study of a low-scale walking Technicolor model with ρ_T and a_T production in the fully leptonic final state at 95% C.L. in proton-proton collisions at $\sqrt{\mathrm{s}} = 10$ TeV scenario using Monte Carlo simulation. We conclude that such processes can be excluded with 366 pb^{-1} of data for ρ_T masses up to 400 GeV and the observation would require 2.8 fb^{-1} of data with 5 σ precision.

DIBOSON PHYSICS WITH CMS DETECTOR

by

IRAKLI SVINTRADZE

B.S. Tbilisi State University, Republic of Georgia, 2002

A DISSERTATION

submitted in partial fulfillment of the
requirements for the degree

DOCTOR OF PHILOSOPHY

Department of Physics
College of Arts and Sciences

KANSAS STATE UNIVERSITY
Manhattan, Kansas
2013

Approved by:

Major Professor
Yurii Maravin

Abstract

In this dissertation, you will find a study of di-boson production in pp collision with the Compact Muon Solenoid (CMS) detector at Large Hadron Collider (LHC). A study of $\mathrm{Z}\gamma \rightarrow \mu\mu\gamma$ process is performed on the data collected by the CMS during 2011 and corresponding to integrated luminosity $\mathcal{L}$= 5 fb^{-1}. The study consists of two parts: cross section measurement and setting the limits on anomalous trilinear gauge couplings (aTGC) between a Z boson and a photon.

The measured cross-section of $\mathrm{Z}\gamma \rightarrow \mu\mu\gamma$ agrees within the uncertainties with the standard model predicted cross section at next to leading order. Having found no excess in cross section measurement, we set the 95% confidence level (C.L.) limit on aTGC, corresponding to: $|h_3^\gamma| < 0.013$, $|h_4^\gamma| < 0.00012$, $|h_3^\mathrm{Z}| < 0.011$ and $|h_4^\mathrm{Z}| < 0.00011$.

Another study discussed is a study of a low-scale walking Technicolor model with ρ_T and a_T production in the fully leptonic final state at 95% C.L. in proton-proton collisions at $\sqrt{\mathrm{s}} = 10$ TeV scenario using Monte Carlo simulation. We conclude that such processes can be excluded with 366 pb^{-1} of data for ρ_T masses up to 400 GeV and the observation would require 2.8 fb^{-1} of data with 5 σ precision.

Table of Contents

List of Figures

List of Tables

Chapter 1

Introduction

Elementary particles are the basic building blocks of the matter. A branch of physics that studies the properties of elementary particles is called particle physics. These particles interact with each other through fundamental forces. Current understanding on what rules govern such interactions are summarized in the standard model theory (The SM[8]). The SM was developed in early 70s, when scientists proposed the idea that matter was made of leptons and quarks, followed by a theory to unify electromagnetic and weak forces into single force also referred to as the electroweak force. This theory gained popularity over time, as it successfully predicted the existence of a number of particles, such as $W^{\pm}$, Z, Higgs bosons, etc. It has been tested by many experiments, and all existing data agreed well with the SM predictions. Despite this fact, the SM theory has no answers to some of the fundamental questions such as: what is the origin of dark energy and what are the constituents of dark matter? What is the origin of a mechanism that caused such a drastic imbalance between matter and anti-matter? What is the origin of a mass hierarchy between different particles? and many others.

Because of these questions, it is believed that the SM is a part of more general theoretical model, search of which serves as a motive for ongoing experiments. If the SM is really a low-energy of more general theory, one would expect new particles predicted by these complex theories to exist in the nature, in other words, there must be a scale at which the SM is not valid. New laboratories are built to increase the energy frontier of particle collisions, and more theories are developed that might shed the light on the fundamental problems. Exceptionally remarkable machine called the Large Hadron Collider (LHC[9]) was built to test validity of the SM theory. The main target for the LHC is the discovery of the Higgs boson, that would explain how the elementary particles acquire masses. There are two large general-purpose detectors at the LHC - Compact Muon Solenoid (CMS[10]), and A Toroidal LHC Apparatus (ATLAS[11]). These detectors were built to detect any new particles that could be produced in proton-proton collisions at the LHC. According to recent studies at the CMS and ATLAS detectors observed a new boson particle, which is consistent with the SM Higgs boson[12,13]. If new boson is really a SM Higgs boson, this would once more confirm the validity of the SM theory.

With a discovery of the new boson, it is necessary to study boson couplings, as a test of

the electroweak sector of the SM. Di-boson physics play an important role as it connects the Higgs mechanism with the gauge boson self-interactions, that can be studied with diboson processes. This thesis is a mix of different studies aimed to aid the study or test electroweak sector of the SM theory with two bosons in a final state. The work is organized as follows:

- The description of the theoretical aspects and the motivation for the analyses is described in Chapter 2.
- An overview of the large hadron collider and the detailed description of the main parts of the compact muon solenoid detector is described in Chapter 3.
- In Chapter 4 I describe methods to identity final state particles with the CMS detector.
- Events containing a photon in the final state are of a special interest in di-boson physics. A measurement of the Zγ processes, where a Z boson decays into a pair of muons is described in Chapter 5.
- A procedure of limits setting on the anomalous trilinear gauge couplings is described in Chapter 6.
- A Monte Carlo (MC) simulation based study, that estimates the amount of data needed for exclusion by the 95% C.L. various mass points of a low-scale walking Technicolor models, such as a ρ_{T} and a_{T} production using the $\rho_{\mathrm{T}}/a_{\mathrm{T}} \to \mathrm{WZ} \to \ell\ell\ell\nu$ final state in proton-proton collisions at $\sqrt{\mathrm{s}} = 10$ TeV is provided in Chapter 7.

Chapter 2

Theoretical Model

2.1 The Standard model

The standard model is the theory that describes how the fundamental particles interact with each other. There are 17 particles in the SM, 12 out of which are constituents of matter and are called fermions, and the rest five serve as mediators of forces and are called bosons.

Fermions are divided into two groups, each consisting of six members. One of the groups consists of quarks. They bind together in either triplets or doublets, further classifying fermions into baryons and mesons, respectively. The remaining six fermions are called leptons. They do not need to bind together and can exist on their own. It's worth mentioning that neutrinos are a special group of leptons. Due to their small mass, they hardly interact with matter and are difficult to detect. The Tau neutrinos were discovered only in the year of 2000. Fermions are further divided into three generations. First-generation fermions usually form a stable particle (atoms, protons, etc.), while the second and the third-generation fermions form unstable particles. Unlike leptons, quarks carry fractions of elementary charge, and when they bind they make group with a total charge to be multiple of elementary charge. Quantum electrodynamics (QED) describes the interaction between charged particles through the exchange of photons. In addition, quarks differ from lepton by a property called color. Colored particles interact with each other through the exchange of gluons, and this interaction is described by quantum chromodynamics (QCD[14]). Another property of fermions is flavor, and interaction between flavored particles is described by weak force through the exchange of intermediate vector bosons (W and Z). In high-energy physics, it is convenient to merge electromagnetic and weak forces under electroweak (EWK) force.

Each of the forces is described by the gauge theory of its own symmetry group - strong - SU(3), weak - SU(2), and electromagnetic -U(1). The SM theory is non-Abelian gauge theory with U(1)×SU(2)×SU(3) symmetry group. SM doesn't include gravity force, as its mediator (graviton) has not been yet observed. The summary of the SM particles is illustrated in Figure 2.1.

The masses of the gauge bosons are very different. This phenomena is called electroweak

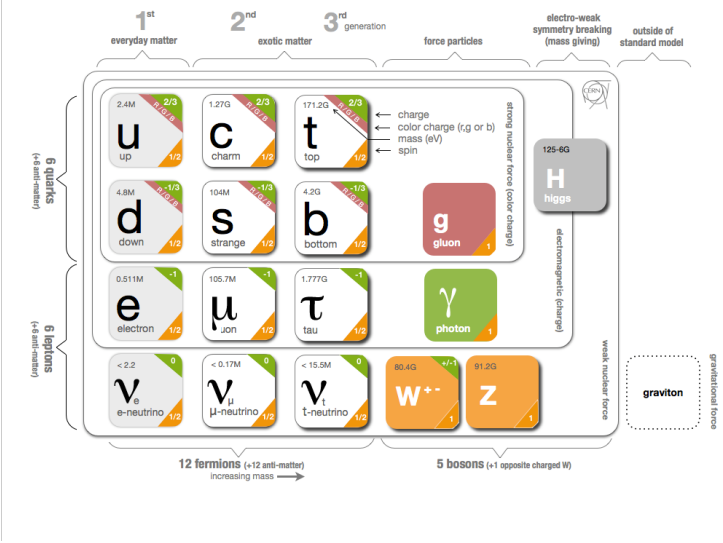

Figure 2.1: The summary of elementary particles[1].

symmetry breaking. For many decades, physicists around the world were puzzled about the mechanism responsible for the differences between massless photons, gluons and massive W and Z bosons.

There are a number of ways that can explain electroweak symmetry breaking. One of these ways is to introduce yet another particle, a Higgs boson (H[15]). This particle is a mediator of Higgs field and all particles with mass directly interact with this field. Through this interaction, particles acquire their masses, including the Higgs boson particle itself as it is allowed to self-interact. This way, the Higgs mechanism explains mass differences of particles in the SM. In 2012, the LHC first claimed the discovery of a new boson particle that looks like a long hunted Higgs boson particle. This most likely will mean the Higgs mechanism to complete the SM.

Another theoretical development that explains EWK symmetry breaking is physics beyond standard model (BSM[16]). One of the branches of BSM is Technicolor[17] theory, which was inspired by QCD. Instead of introducing elementary Higgs boson particle to explain observed phenomena, Technicolor model generates masses of the W and Z bosons by hypothesizing a new gauge interaction coupled to massless fermions.

2.2 Physics with two bosons

As of today, most of the existing physics models in hadronic collisions, would it be non SM Higgs mechanism, SUSY, or various extensions of SM, predict processes with new physics phenomena that are very likely to decay into two bosons. Hence, extensive and thorough studies of gauge boson production can, not only provide important tests of the electroweak sector of the SM, but also possibly lead to a discovery of the new particles, not necessarily

predicted by the SM.

Di-boson processes are very likely to involve a W and Z gauge bosons. The properties of these gauge bosons have been explored in details with previous experiments and repeated by CMS experiment[18]. Both gauge bosons decay into hadrons for about 70% of the time. A Z boson decays into charged leptons for about 10% of the time (W -30%), and because this vector boson has an easily identified leptons and virtually background free - it is commonly used also for detector calibration purposes and is often mentioned as a standard candle. Additionally, unlike W and Z bosons, a photon doesn't decay into other particles. The couplings between gauge bosons are of particular interest.

Some of the couplings are allowed within the SM, but some of them are restricted. Processes where particles directly interact with each other are described with a so-called tree level Feynman diagrams, and calculations that include these processes are called leading order calculations (LO). The process when the interaction is usually accompanied by the exchange of a virtual particle is described by loop Feynman diagrams and corresponding to it calculations are mentioned as next to leading order (NLO). Figure 2.2 illustrates these two types of processes. Gauge bosons are allowed to self-interact at a tree level, with the restriction, that it can only happen between charged and neutral gauge bosons.

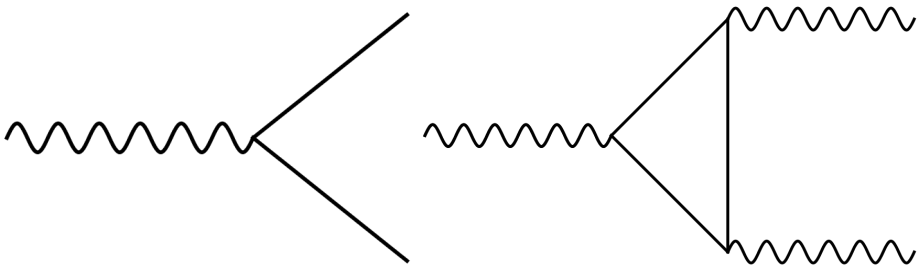

Figure 2.2: Feynman diagrams illustrating a tree level interaction (left) and a single loop interaction (right).

2.2.1 SM Zγ production and anomalous trilinear gauge coupling

In the SM, a Z boson and a photon do not self-interact, in other words, we can say that anomalous trilinear gauge couplings, ZZγ and Z$\gamma\gamma$, are zero. Figure 2.3 illustrates possible interactions of Z$\gamma \to \ell\ell\gamma$ process (ℓ stands for lepton). The process when interacting parton emits a photon is called initial radiation (ISR) and the process when a lepton from a Z boson emits a photon is called final state radiation (FSR). The only non-negligible background process for this channel is the Z boson production associated with hadrons, where neutral and charged particles coming from hadronization easily mimic a photon.

The most general parameterization of interaction between a Z boson and a photon is expressed by constructing the Lorentz and gauge invariant ZVγ vertex, illustrated in Figure 2.4. Here, V can be either a Z boson or a photon. The circle includes various tree level and loop contributions to the ZV coupling making the approach model independent. This

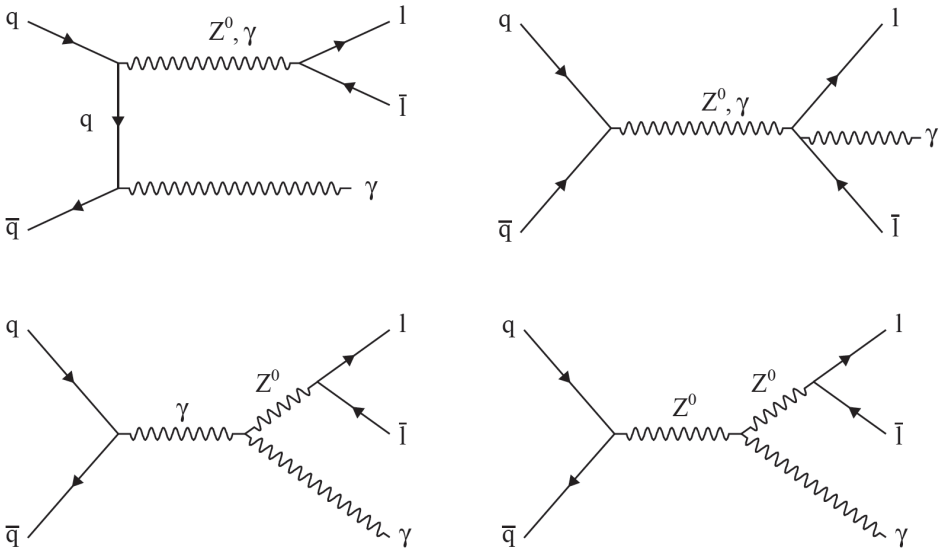

Figure 2.3: Feynman diagrams of $Z\gamma \to \ell\ell\gamma$ illustrating initial and final state radiation[2] (top left and top right) and the $Z\gamma\gamma$ and $ZZ\gamma$ trilinear gauge couplings (bottom left and bottom right).

most general coupling can be parameterized by four complex coupling parameters[19]. The $ZZ\gamma$ vertex function is defined in Equation 2.1 and $Z\gamma\gamma$ vertex can by obtained by following substitution described in Equation 2.2.

$$\Gamma^{\alpha\beta\mu}_{ZZ\gamma} = \frac{P^2 - q_1^2}{m_Z^2}(h_1^Z(q_2^\mu g^{\alpha\beta} - q_2^\alpha g^{\mu\beta}) + \frac{h_2^Z}{m_Z^2}P^\alpha[(P\cdot q_2)g^{\mu\beta} - q_2^\mu P^\beta] + h_3^Z\epsilon^{\mu\alpha\beta\rho}q_{2\rho} + \frac{h_4^Z}{m_Z^2}P^\alpha\epsilon^{\mu\beta\rho\sigma}P_\rho q_{2\sigma}) \tag{2.1}$$

$$\frac{P^2 - q_1^2}{m_Z^2} \to \frac{P^2}{m_Z^2} \text{ and } h_i^Z \to h_i^\gamma,\ i = 1, ..., 4. \tag{2.2}$$

The effects of anomalous trilinear gauge couplings (aTGC) in $Z\gamma$ production can be observed as an increase of $Z\gamma$ differential cross-section and show up as excessive events at the high end of transverse energy of the photon, illustrated in Figure 2.5. Observation of anomalously high gauge boson production could possibly indicate the presence of new physics. For example, there are several theories predicting aTGC: a minimal super-symmetric standard model (MSSM[20]) with heavy SUSY particles that enhances coupling; alternatively, the theory that predicts a composite Z boson[21] consisting of point-like hypothetical particles like preon and anti-preon, etc. Neither of these particles has been yet observed.

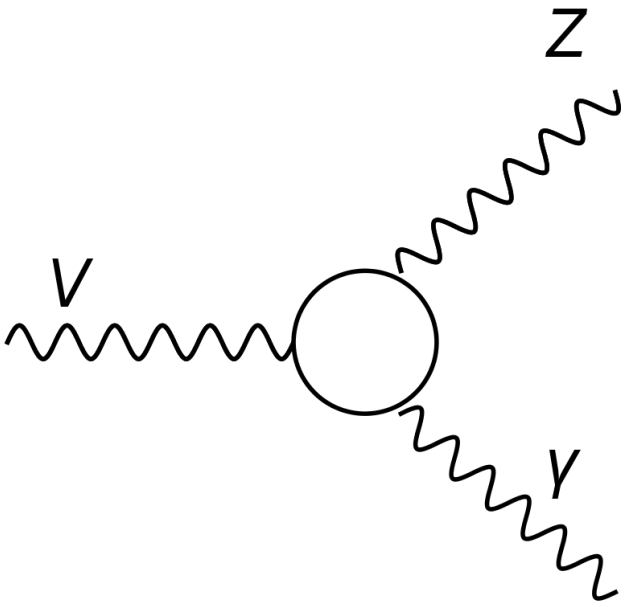

Figure 2.4: ZVγ general vertex.

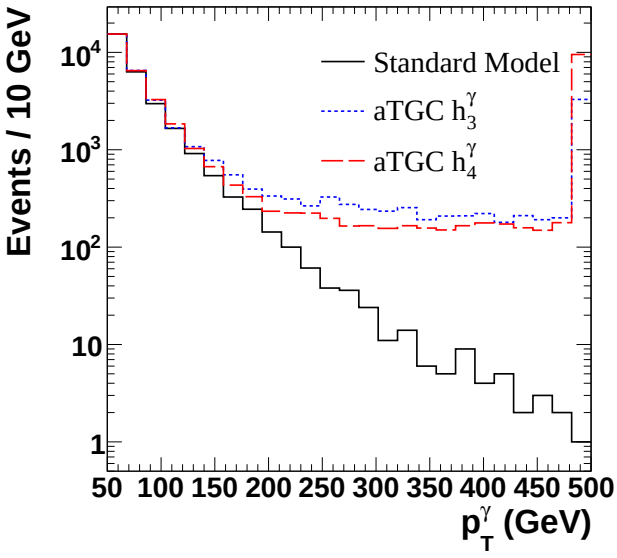

Figure 2.5: MC generator level photon transverse momentum distribution comparison between SM (solid line) and two aTGC points with non zero h_3(dotted line) and h_4(dashed line) parameters. Differential cross section is enhanced on high transverse energy of a photon due to aTGC.

2.2.2 Technicolor decaying into WZ

The most-recent versions of Technicolor[17] theory enable so called "a slowly running" or "walking" gauge couplings to break down electroweak symmetry and keep the unwanted flavor changing neutral current interactions evaded. As a result, this theory predicts a techni-particles ρ_{T} and a_{T}, that could masses as low as 300 GeV and their decay channels (e.g. $\rho_{\mathrm{T}}/a_{\mathrm{T}} \rightarrow \mathrm{WZ}$) have a narrow resonance peak, illustrated in Figure 2.7. The ρ_{T} and ρ_{T} are produced through quark annihilation into an intermediate W^* boson. As a result, the final state objects consist of three leptons and a neutrino, see Figure 2.6. As of today, none of Technicolor particles has been observed.

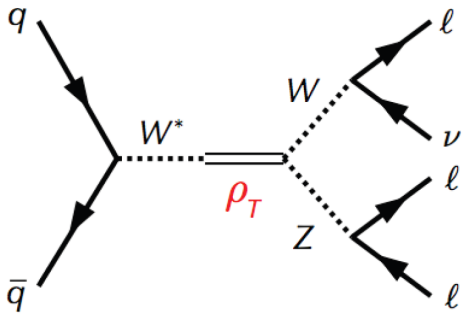

Figure 2.6: Feynman diagram of $\rho_{\mathrm{T}}/a_{\mathrm{T}} \rightarrow \mathrm{WZ} \rightarrow \ell\ell\ell\nu$[3].

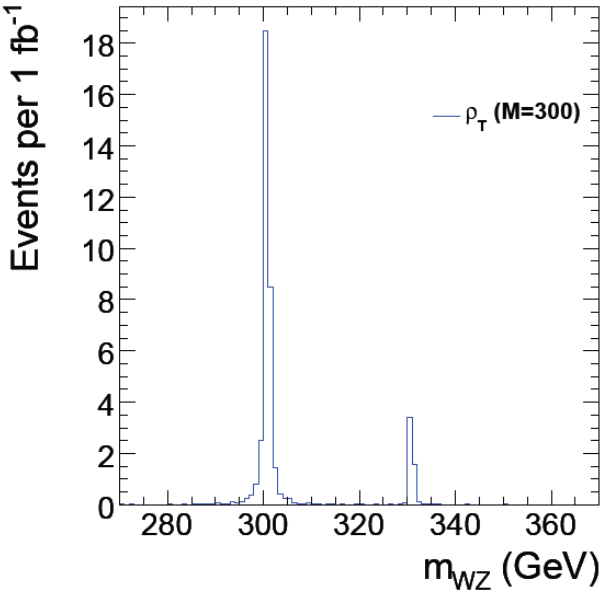

Figure 2.7: Generator level WZ invariant mass distribution for ρ_{T}[3].

2.2.3 The Higgs boson production

A SM Higgs boson is a gauge mediator of a Higgs field, latter is the simplest mechanism to explain the electroweak symmetry breaking. Finding the Higgs boson is one of the major goals of the LHC. There are a number of channels, that the Higgs boson decays to, making di-boson physics even more interesting (for example $H \to \gamma\gamma$, $H \to ZZ$, $H \to WW$, $\rho_T/a_T \to WZ$). Figure 2.8 illustrates branching fractions of the SM Higgs decay channels. Many of these channels have been studied for the Higgs production very recently, but results will not be discussed here.

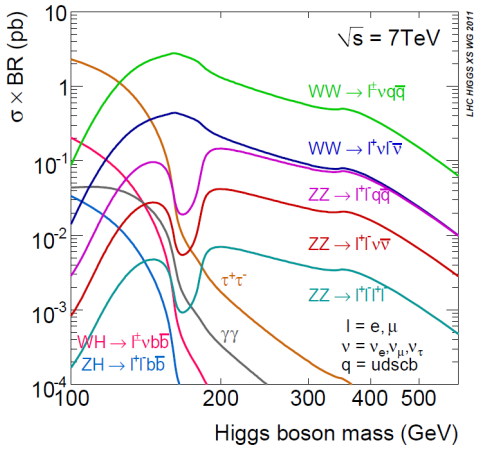

Figure 2.8: A Higgs boson production branching fractions as a function of mass of H[4].

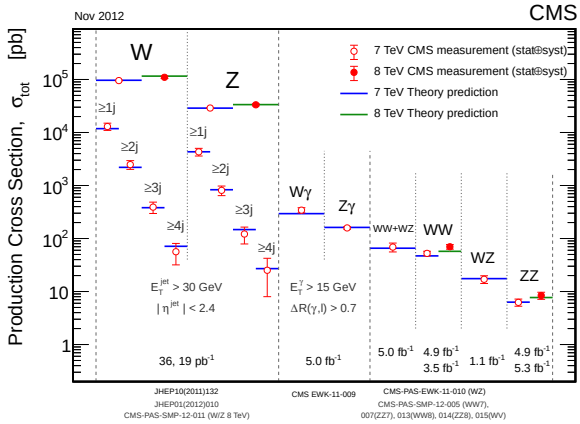

Figure 2.9: The results of measurements carried out by CMS in SM EWK production illustrate agreement between observation and theoretical prediction[5].

2.2.4 CMS results of SM measurements

Currently, the CMS collaboration published hundreds of papers. The results of the SM process measurements are illustrated in figure 2.9. The measurements of SM production cross sections performed by the CMS agree with the theoretical predictions. The details of my contributions to one of those measurements (for $Z\gamma$) are described in chapter 5.

Chapter 3

The Large Hadron Collider and Compact Muon Solenoid Detector

3.1 The Large Hadron Collider

The Large Hadron Collider (LHC[9]) is accelerator complex consisting of two superconducting rings circulating proton beams in opposite direction. It is located on the border of France and Switzerland at the European Laboratory for Particle Physics Research (CERN). By original design LHC has to collide the beams of protons at a center-of-mass energy of $\sqrt{s} = 14$ TeV with a nominal instantaneous luminosity of $\mathcal{L} = 10^{35}$ cm^{-2}s^{-1}. Currently it is operating on $\sqrt{s} = 8$ TeV and $\mathcal{L} = 5 \times 10^{33}$ cm^{-2}s^{-1}. The main purpose of LHC is to search for the production of Higgs boson or any new particle with mass up to 1 TeV. Two experiments have been installed around the LHC to pursue these results: ATLAS[11] and CMS[10]. Additionally, LHC hosts other experiments like LHCb[22] and ALICE[23], which study the properties of hadrons.

The LHC was installed in the 26.7 km circumference tunnel originally used by the Large Electron-Positron (LEP) collider. On contrary to LEP, LHC can achieve energies on the order of TeV, thanks to massive charged particles - protons; heavy nuclei radiate less energy compared to electrons. To achieve the highest possible collision energy, protons are first injected into the proton synchrotron (PS) and accelerated to 25 GeV. Next, they are injected to the super proton synchrotron (SPS) and further accelerated to 450 GeV. Finally, beams are injected into the LHC, and circulate in opposite directions, while being accelerated to the nominal energy. Super-conducting dipole magnets, each 15 m long, deliver a 8.3 T magnetic field, that allows the beams to circulate in vacuum pipes. The LHC complex diagram is illustrated in Figure 3.1

The LHC started its operations in December 2009 with $\sqrt{s} = 0.9$ TeV. In 2010; the center of mass energy was set to 7 TeV and the performance during 2010, and 2011 raised impressively. The peak instantaneous luminosity reached $\mathcal{L} = 2 \times 10^{32}$ cm^{-2}s^{-1}, short after, in 2011, it was increased by the factor of ten $\mathcal{L} = 3.5 \times 10^{33}$ cm^{-2}s^{-1}. Same year, LHC managed to deliver data of about 5 fb^{-1} integrated luminosity.

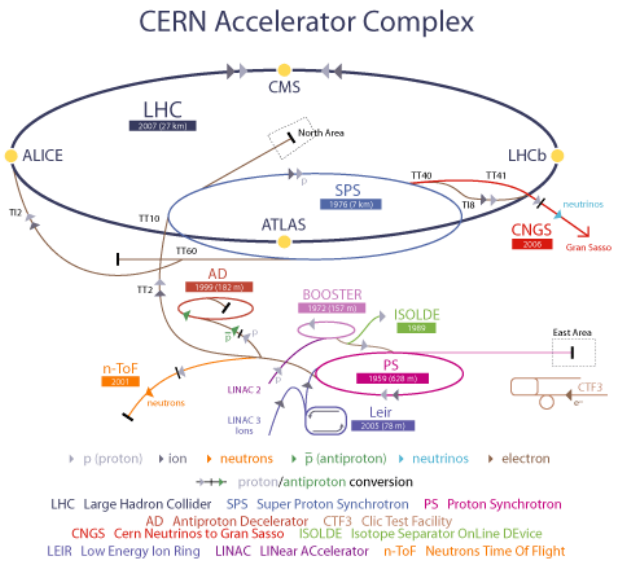

Figure 3.1: The LHC accelerator complex[6].

3.2 The Compact Muon Solenoid

The Compact Muon Solenoid (CMS) is a general-purpose detector housed at interaction point 5 of the CERN Large Hadron Collider. It is designed around a 4 T magnetic field provided by the largest superconducting solenoid ever built. The structure of CMS is illustrated in the Figure 3.2. The CMS detector consists of following subsystems: tracker (silicon Pixel and Strip subdetectors), calorimeter (Electromagnetic and Hadronic subdetectors), and muon detector.

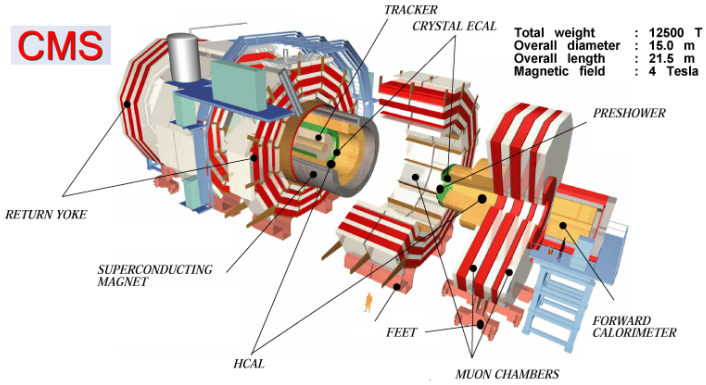

Figure 3.2: The CMS detector[7].

The events are described in the reference frame located in the geometrical center of CMS detector. The coordinates are described either in Cartesian or polar coordinates with

respect to origin:

- In Cartesian coordinate system - x axis points towards the center of the LHC ring, y axis points upwards, perpendicular to the LHC plane, and z axis points along the beam like, completing the right-handed reference.
- In a polar coordinate system, the directions are defined with angles ϕ, and θ, where $\tan\phi = \frac{y}{x}$ and $\tan\theta = \frac{\rho}{z}$
- From the polar angle, the rapidity y, and pseudo-rapidity η are obtained.

$$y = \frac{1}{2}\ln(\frac{E + p_z}{E - p_z}) \tag{3.1}$$

$$\eta = -\ln(\tan\frac{\theta}{2}) \tag{3.2}$$

  In high-energy physics, it is common to use pseudo-rapidity, as this angle is Lorentz invariant under longitudinal boost. This helps to define distances ΔR between two objects in the (η, ϕ) plane.

3.2.1 The Magnet

The CMS detector is designed around a 4 T superconducting solenoid, which is 12.5 m long and has the inner radius of 3 m, and it can store up to 2.6 GJ of energy. The field is closed by the return yoke, which consist of five barrel and two end-cap pieces, composed of three layers each. The magnet is designed in such a way that it helps to measure the muon momentum precisely. A solenoidal field bends the particles in transverse plane and allows for better measurement of vertex position, where the particle was originated from. The size of the solenoid allows efficient muon detection and measurement up to a pseudo-rapidity $|\eta| < 2.4$. The size of the magnet allows housing the tracking and calorimetry systems inside of it. Currently, the magnet is operated at 3.8 T.

3.2.2 The Tracker

The tracker system is located in the core of the CMS detector. It measures 2.5 m in diameter and 5.8 m in length. The purpose of the tracker is to provide a precise and efficient reconstruction of the charged particles emerging from pp collisions. It also allows to reconstruction the secondary vertices. The CMS Tracking System is composed of two parts: The Silicon Pixel detector and Silicon Strip Detector. The Pixel Detector is divided into three barrel layers and two disks in each end-cap, while the Strip detector consists of two main parts - an inner and outer tracker. Inner tracker has four barrel layers and three end-cap disks, and outer tracker has six barrel layers and nine end-cap disks. Furthermore, it is the world's largest tracker with active silicon surface of about 200 m^2.

The high reliability, efficient and precise reconstruction of the charged particle trajectories (tracks) carry a crucial role in CMS detector, mainly because this information is heavily used by the triggering system, that reduces the rate of event collection from the 40 MHz down to less than 100 Hz. None less importance has the exact reconstruction of the secondary vertices in the event, as this information is used in the searches for short lived exotic particles. Additionally, tracker completes the functionality of calorimeters and muon systems to help identifying the objects of interest.

3.2.3 The muon spectrometer

The muon spectrometer is a system of sub-detectors with different technologies, rather than being a single detector. Unlike the electromagnetic and hadronic particles, which are mainly contained inside the calorimeters, muons are able to travel through the solenoid without much energy loss. Muons with high transverse momentum, that originated from the collision, are rather background free, also, just like any other leptons, they are likely to provide interesting events with the indication of new hypothetical particles. Due to this, muons are of a particular interest for the triggering purposes. The muon sub-detector is composed of three types of gaseous detectors. Most of the sub detectors are housed within hollow spaces of the iron yoke, and because of this, the segmentation closely follows the same structure. In the barrel region, the standard drift chambers with rectangular cells are used. The barrel drift tubes (DT) cover the pseudo-rapidity region up to $|\eta| < 1.2$, and it is divided into four stations. The first three stations contain chambers layered in two and provide the precise momentum measurement in the transverse plane, while the fourth station measures momentum along z axis. To avoid any inefficiencies in muon reconstruction, the cells in each layer are shifted by the half of their width.

In the high pseudo-rapidity (forward) region, the particle production rate is higher compared to the central region. The choice for muon detector fell upon cathode strip chambers (CSC), because of their fast response time, fine segmentation and radiation tolerance. Each end-cap is equipped with four stations of CSCs that cover the $0.9 < |\eta| < 2.4$ pseudo-rapidity range. The cathode strips are oriented radially, while the anode wires run perpendicular to the strips. The muon reconstruction efficiency is typically very high, overall of about 95-99%. Both the DTs and CSCs can trigger on muons in a level 1 trigger with muon p_{T} resolution of 15% and 25%, respectively. Additionally, trigger dedicated muon detectors were added to help with measuring the correct beam-crossing time - Resistive Plate Chambers (RPC); gaseous detector operated in the avalanche mode, which can provide an independent and fast trigger with high segmentation and sharp p_{T} threshold over a wide range of pseudo-rapidity.

3.2.4 Calorimetry

As in most of the particle physics experiments, calorimetry is distinguished between electromagnetic and hadron calorimetry. Identification of electrons and photons highly depend on

the resolution of calorimetry. Calorimetry process is destructive; electromagnetic calorimetry is sensitive to the production of the electromagnetic showers inside the absorber material, and hadron calorimetry is based on effects from inelastic scattering of heavy nuclei, including pair production of photons from neutral pions or leptons.

The electromagnetic calorimeter (ECAL) of CMS is homogeneous and is composed of 61,200 lead tungstate ($PbWO_4$) crystals in the barrel region and 7,324 crystals in the end-caps. The ECAL end-caps are additionally equipped with a pre-shower detector. The ECAL crystal has a front-face with a dimension of 22x22 mm, and measures 230 mm in length. $PbWO_4$was chosen because of its high density and short radiation length. Properties of crystal allow the calorimeter to be put compact, while providing a high granularity. Additionally, the scintillation and optical properties of $PbWO_4$ make ECAL fast and radiation tolerant. Scintillated light is detected with two different technologies - Avalanche photo-diodes (APD) are used in the barrel region, and Vacuum photo-triodes (VPT) are used in the end-caps (mainly because they are more radiation resistant compared to APD). The pre-shower detector is a sampling calorimeter made of lead radiators and silicon strips, purpose of pre-shower is to help identifying the neutral pions in the forward region.

The purpose of the hadron calorimeter (HCAL) is to measure the energy and direction of hadron jets, also additionally it provides information about neutrinos. The hadron calorimeter is constrained in inner radius by ECAL and in outer radius by the solenoid, meaning that existing absorber material inside this space is not always enough fully measuring hadronic showers. Because of this, an outer HCAL layer is located outside of the solenoid to collect the remaining tails. The pseudo-rapidity coverage is extended in the $3 < |\eta| < 5.2$ by forward Cherenkov-based calorimeters, high pseudorapidity coverage helps measuring the missing transverse energy. The barrel part (HB), consists of 36 wedges made of brass absorber layers. The maximum material amount in both HB and HE corresponds to approximately 10 interaction lengths λ_I .

3.2.5 The trigger

The protons in the LHC ring are traveling nearly the speed of light, hence they circle 27 km circumference 11000 times a second. Additionally, protons travel in bunches, and their total rate of interactions per second is so huge that no electronics can keep up with speed to record each event. In order to achieve reasonable data taking rate, a triggering system is used in multiple steps to select only the events that contain useful information for the physics analysis. The decision, whether the event is of a particular interest is made by the algorithm divided into two steps: the level-one ('L1') trigger, followed by a higher-level trigger (HLT). Data taking rate is reduced by the 'L1' trigger from about 1 GHz to less than 100 kHz, latter is further reduced by HLT down to 500 Hz. HLT utilizes full detector reconstruction techniques to identify the object of interest and reduce the background rates. The events that pass HLT real-time selections are stored on the tape and analyzed later.

'L1' trigger relies on the information from the calorimeters and the muon detector, and based on pattern recognition techniques it determines whether the event contains any leptons, jets, or missing transverse energy, or any combination of these. In general, sub-

detectors have their own dedicated triggering systems, for example, muons have DT Trigger system in the barrel, the CSC trigger in the end-cap and the RPC trigger covering both barrel and end-cap for further support; these systems are later centralized with the 'L1' muon trigger that combines the results from all three triggering systems to form a more solid - a global muon trigger candidate. Similarly, a global calorimeter trigger takes into account the information from ECAL, and HCAL triggers. Tracker, unlike the other systems, doesn't have dedicated 'L1' triggering system. The full information about the detector at the moment when either of triggers flagged the event as interesting is saved to Data-Acquisition system (DAQ) for further processing with HLT. At last, HLT sequence fully reconstructs the event at local computer-farm using real-time processing with predefined algorithms. For example, muon HLT path takes initial seeds from 'L1' triggers, matches them to available tracks, fully and efficiently reconstructs high p_{T} muon candidates, applies the pre-identification criteria, thus improving the energy resolution and providing a better rejection power (i.e. removes objects that mimic muon). HLT triggers are highly configurable, for example, CMS utilizes dedicated triggers to select the Z bosons with high purity - since high p_{T} lepton pairs that compose a high invariant mass candidate are rare and difficult to fake.

Chapter 4

Data Analysis Techniques

The events that pass the pre-selection of the predefined trigger paths are recorded to mass storage for further analysis. The information from all the sub-detectors contain a full description of the event, but the detector response must be analyzed in details in order to get objects of interest, such as leptons and photons. This process is referred to as 'reconstruction'.

4.1 Muon Reconstruction

Muons are reconstructed mainly using the tracker information and by including the additional information from the muon sub-detectors. CMS have three methods of reconstructing muons:

- Tracker muon algorithm is designed to search for low p_{T} muons. Thus, it starts from track candidates within the silicon strip tracker, propagates the track fit into the muon sub-detector system, and searches for any segments that match the propagation region within the error. If at least one corresponding hit is found, the candidate is considered to be a muon.

- Stand-alone muon algorithm starts from reconstructed muon candidates from muon system and requires propagated track to come from the interaction point. By design, Stand-alone muons are not suited for the low p_{T} muons, as it requires at least two segments in muon chambers to form a track in initial muon candidate, i.e. some of the low p_{T} muons never even reach that far out or curls in the magnetic field..

- The global muon algorithm starts with the stand-alone muon algorithm and propagates the stand-alone muon track to the innermost surface of the calorimeter. A matching track in the silicon is searched for within the errors in position and energy of the propagated stand-alone track. If a track is found within the search window, it is combined with the muon system track. The tracking information from both detectors is then used in a global track fit, improving momentum resolution for a high muon p_{T}.

More details about muon reconstruction and its performance can be found in official muon reconstruction Physics Analysis Summary (PAS)[24].

4.2 Photon reconstruction

In CMS, the photons are reconstructed using the energy deposits in ECAL. Usually, most energy of the photon (97% for unconverted) is contained with 5x5 crystals around the most energetic crystal (referred to as 'seed'). Photon candidates are formed by "SuperCluster" (SC) algorithm that uses the energy deposits in 5x5. Furthermore, sometimes photons convert due to the material budget (tracker) right in front of the ECAL; they produce an electron-positron pair, which bend in the magnetic field in ϕ direction and make photon energy recovery a little trickier business. For the converted photons (one can usually tell from the fraction of energy in 3x3 around the seed to the 5x5 crystals is less than 95% due to the Moliere radius), 5x5 region is extented in ϕ to include the region with up to 17 crystals. This ensures that all energy spreads of the photon is collected by the algorithm. The energy of the photon is typically corrected as a part of reconstruction, and this correction is at the order of 1%, and vary with the E_{T} and η of the photon. Additionally, loose identification requirements are imposed during the reconstruction of the electron to improve purity of the selected candidates. For example, the ratio of HCAL energy behind a SC, 'H/E' , being less than 0.15 is used to reject ECAL deposits that clearly come from jets. More details about photon reconstruction and its performance can be found in official photon reconstruction and identification PAS[25].

Chapter 5

Zγ cross section measurement

5.1 Introduction

I am one of the authors of $V\gamma$ paper (soon to be public), contents from this dissertation closely follows the structure of the related internal CMS note[2], available upon request. I will concentrate more on my contribution, which is cross section measurement of the Zγ production with the Z boson decaying to the pair of muons.

The following cuts are used to define the phase space, in which we measure the cross section:

1. photon $E_{\mathrm{T}} > 15$ GeV
2. Seperation between leptons from Z boson decays and a photon should be $\Delta R(\ell, \gamma) > 0.7$
3. The invariant mass of the Z boson should be above 50 GeV.

The reason behind this is to avoid the divergence of the cross section on radiated photon collinear to Z lepton and photons with low p_{T} in MC samples.

5.2 Data samples

The data used in this analysis corresponds to integrated luminosity $\mathcal{L}= 5$ fb^{-1} in pp collision at $\sqrt{\mathrm{s}} = 7$ TeV, collected by CMS detector in 2011. The data sample is processed with standard data quality criteria, recommended by CMS, in order to avoid the portions of the data affected by sub-detector problems. In this case, all events for analysis must be declared as usable for physics by muon and ECAL detector quality control groups.

5.3 Monte Carlo samples

The Zγ production is modeled by the number of generator - MadGraph5[26], Monte Carlo for FeMtobarn generator (MCFM[27]), Sherpa[28]. For this study, the LO with up to 2 partons

was generated to model Zγ signal using MadGraph5 generator. The sample is normalized to be corresponding to the study integrated luminosity using the NLO cross section calculated from MCFM.

To avoid the migration effects related to the energy scale/resolution of lepton/photon and reconstruction inefficiencies - the signal sample was generated using following generator cuts: $E_{\mathrm{T}}^{\gamma} > 10$ GeV, $|\eta^{\ell}| < 10$, $|\eta^{\gamma}| < 10$, $p_{\mathrm{T}}^{parton} > 10$ GeV, $m_{\ell\ell} > 40$ GeV, and a separation between a photon and final state muon $\Delta R(\mu, \gamma) > 0.6$. The corresponding to this sample NLO cross section, calculated by MCFM, is 12.3 pb^{-1}.

To model the background, we use a list of already existing MC samples, recommended by CMS for data analysis, tables 5.1 contains also corresponding cross sections.

Table 5.1: Summary of Monte Carlo background samples used. Left column shows the process name, and right column corresponding to sample cross section. * means the sample is a set of subsamples that are binned in tree level parton momentum $\hat{p_{\mathrm{T}}}$, see the details in the original note.

Process	σ, pb
$\mathrm{Z}\gamma \to \tau\tau\gamma$	45.2 (NLO)
$t\bar{t} + jets$	165 (NNLO)
$t\bar{t} + \gamma$	0.444 (LO)
WW	5.7 (NLO)
WZ	18.2 (NLO)
ZZ	5.9 (NLO)
$DiPhoton + jets$	190.56 (NLO)
$\gamma + jets$	*
QCD	*

All the samples are generated in such way that they support pile-up effects that present in the data, also additional reweighing is done to match the Simulation in all the above mentioned samples also consider a pile scenario with 50 ns bunch spacing with out of time pile up, as it is in real data. With the increase of instantaneous luminosity in the middle of the run, the pile up also increased, thus we will also monitor some key distribution for Run A (before the increase) and Run B (after $\mathcal{L}$ increased) seperately.

5.4 Object and event selection

Triggers

We are using the double muon triggers that select the Z boson events with high purity. This trigger path requires to have 2 well reconstructed global muon triggers, with high enough p_{T} threshold to avoid background rates, but low enough to keep a good recording rate of the Z boson signal. We do not trigger on photon, as the background rates are very high, especially on the low p_{T}.

Description	criterion
Kinematic (loose)	$p_{\mathrm{T}} > 20$ GeV and $\lvert\eta\rvert < 2.4$
Kinematic (tight)	$p_{\mathrm{T}} > 35$ GeV and $\lvert\eta\rvert < 2.1$
Number of pixel hits	> 0
Number of tracker hits	> 10
χ^2/n.d.f	< 10
Number of muon hits	> 0
Number of chambers with matched segments	> 1
vertex d_0	< 0.02 cm
vertex d_z	< 0.1 cm
combined relative isolation	< 0.1

Table 5.2: Muon identification and isolation requirements. The loose selection is used to identify muons from Z boson candidates.

Muon identification and isolation

All muon candidates are required to tracker and global muons, to have high transverse momentum (golden rule is off-line cut should be higher compared to trigger threshold to void turn-on curve). Furthermore, a candidate should be within the acceptance region of the detector. This way, we select high p_{T} muon with a well reconstructed track both in the tracker and in the muon system. The global muon is required to have at least one hit in silicon pixel detector, at least eleven hits in the silicon strip tracker detector, and, at last, at least one hit within the muon system. The vertex the muon originated from should be close to the interaction point. In addition, muon hit quality should be reasonable, and the candidate should be well isolated (shouldn't have significant energy deposition around the candidate in either of sub-detector systems). The summary of the muon candidate selection is listed in Table 5.2.

5.4.1 Tag and Probe

Method Description

One of the important aspects of any analysis is the accurate modeling of MC samples and having a reliable efficiency measurement. In this sub-section, we will describe the procedure, the purpose of which is to identify certain particles in data or MC samples (without relying on MC truth information, as it was a data) and measure the efficiencies of this particle reconstruction and identification. This data-driven approach is also called a "Tag and Probe method" [29].

The "Tag and Probe" method utilizes a mass resonances of knows particles, in this specific case its the Z boson decaying into a pair of leptons. The idea is to select the lepton originating from the Z boson decay and probe the efficiency of a particular selection criterion on this particle. The "tag" is called an object passing very tight selection criteria.

Typically, the Z boson decay in its invariant mass window is virtually a background free, thus there's at least one "golden" lepton that passes tight identification criteria (more than 99%). Once Tag was found in the event, same flavor lepton is required with very loose selection criteria, the latter is called a "probe". Also for every possible Tag and Probe pair we constrain combined invariant mass to be in the window of the Z boson invariant mass range. The definition of the probe criteria depends on the criteria, which we want to measure the efficiency of. The efficiency of this criterion is calculated by estimating the number of "probe" particles passing the selection criteria:

$$\epsilon = \frac{N_{passing}}{N_{all}} \tag{5.1}$$

Where $N_{passing}$ is the number of probes passing the selection criteria and N_{all} is the total number of probes. These numbers are usually obtained from the simultaneous fit on passing and failing probes. Typically, the signal shape is described by a Breit-Wigner distribution convoluted with a Crystal Ball function, where its width is fixed to the width of the Z boson as determined by the Particle Data Group (PDG) global average. The Breit-Wigner function is numerically convoluted with the Crystal Ball function to account for detector resolution and final state radiation effects in the measured distribution. The background is described by a Landau function. The simultaneous fit over failing and passing probe candidates are illustrated in Figure 5.1.

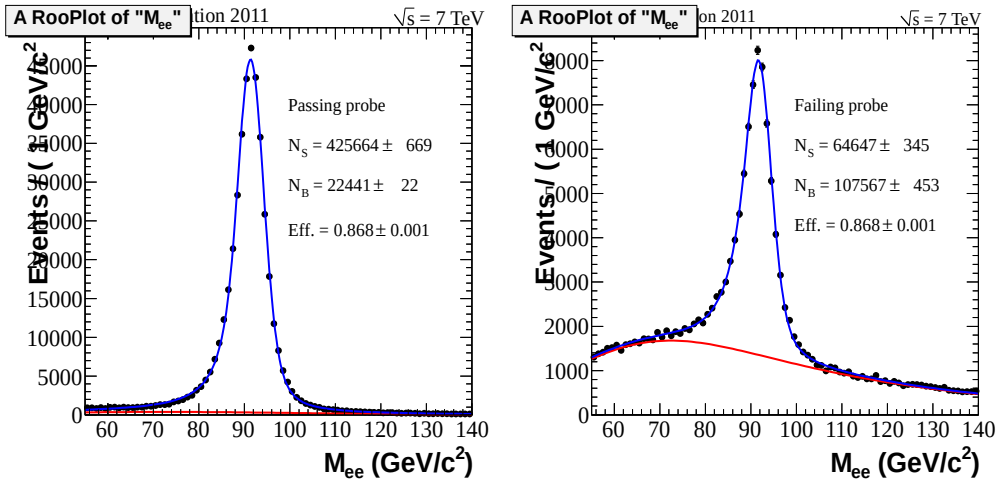

Figure 5.1: The example of fits performed by "Tag and Probe". Left plot shows pair invariant mass with probes passing a selection, and probes failing selection criteria on the right.

Muon Tag and Probe

The performance of the muon triggers, and the overall muon reconstruction criterion is estimated using the tag and probe method.

The overall single muon identification efficiency is factorized as a product of efficiencies of several consecutively applied requirements:

$$\epsilon_{\text{tot}} = \epsilon_{\text{TRK}} \cdot \epsilon_{\text{SA}} \cdot \epsilon_{\text{ID}} \cdot \epsilon_{\text{ISO}} \cdot \epsilon_{\text{HLT}} \tag{5.2}$$

where individual efficiencies are defined below:

- ϵ_{TRK}: The efficiency of reconstructing a track in the Tracker with the required number of pixel and tracker hit
- ϵ_{SA}: The efficiency of reconstructing a track in the muon system, *i.e.*, a stand-alone (SA) muon with at least two muon stations and one matched chamber hit
- ϵ_{ID}: The efficiency of passing the GlobalMuon and TrackerMuon algorithms with the required cuts on $|d_{xy}|$, $|d_z|$ and χ^2/n.d.f
- ϵ_{ISO}: The efficiency of passing the required isolation
- ϵ_{HLT}: The efficiency of satisfying the requirements of the single muon trigger or double muon trigger leg

As the requirements are applied sequentially, the efficiency for both data and MC simulation is estimated with respect to the previously applied criteria. ϵ_{TRK} is approximated by the efficiency of reconstructing a track given a stand-alone muon. As the tag has to fire the HLT trigger whose selection is harder than the hard leg of the double muon HLT trigger. Therefore, checking the probe to pass the di-muon soft leg filter is a measurement of the soft leg efficiency. Both muons in the event have to pass this soft leg filter. Requiring the probe to pass the hard leg filter if a soft leg object has already been matched is a measurement of the hard leg efficiency given the soft leg. This efficiency is measured to be close to one for the used off-line selection.

The tag is defined as a muon that satisfies all muon selection criteria and is matched to a HLT trigger object. The required charge of the tag is selected randomly per event to avoid ambiguousness of the tag selection. The probes are defined to estimate each of the individual efficiencies defined by Eq. 5.2 with definitions and passing criterion summarized in Table 5.3. All probes together with the tag are supposed to have an invariant mass 50 GeV $< M_{\text{TP}} <$ 150 GeV and the opposite charge.

Using Tag and Probe, we calculate the efficiencies as a function of p_{T} and η of the probe and as a function of the number of primary vertices in the event. The latter gives the direct estimate of the pile up dependence. Using this tool, we correct the differences in detector

Table 5.3: Definition of selected probes and the passing criterion.

ϵ	Probe definition	Passing criteria
TRK	SA muon	Track in Tracker
SA	Track in Tracker	SA muon
ID	Track in Tracker and SA muon	Global/Tracker muon
ISO	Global/Tracker muon	Isolated Global/Tracker muon
HLT	Isolated Global/Tracker muon	Isolated Global/Tracker muon matched to HLT

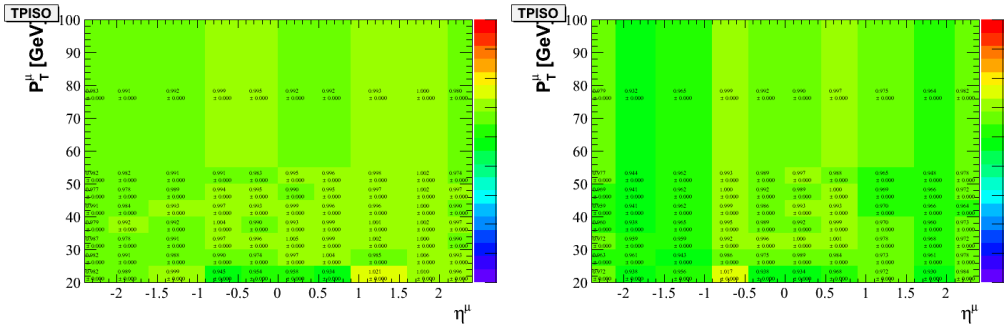

Figure 5.2: Muon efficiency correction maps for run A (left) and run B(right).

Table 5.4: Summary of measured efficiencies of two muons (ϵ^*) with Zγ -selection. MC is adapted to the different pile-up scenarios for Run 2011A and Run 2011B.

Eff. 2 Muons	Data [%]	Monte-Carlo [%]	Data/MC [%]
Run 2011A			
$\epsilon^*_{\mathrm{TRK}}$	98.01 ± 0.01	98.75 ± 0.01	99.24 ± 0.01
ϵ^*_{SA}	94.61 ± 0.02	95.27 ± 0.01	99.24 ± 0.02
ϵ^*_{ID}	98.72 ± 0.01	99.09 ± 0.01	99.63 ± 0.01
$\epsilon^*_{\mathrm{ISO}}$	93.83 ± 0.01	94.10 ± 0.01	99.70 ± 0.01
$\epsilon^*_{TRK,SA,ID,ISO}$	86.88 ± 0.01	87.99 ± 0.01	98.74 ± 0.02
$\epsilon^*_{HLTDoubleMu}$	93.22 ± 0.01	94.93 ± 0.01	98.20 ± 0.01
Run 2011B			
$\epsilon^*_{\mathrm{TRK}}$	97.80 ± 0.01	98.60 ± 0.01	99.20 ± 0.01
ϵ^*_{SA}	91.47 ± 0.02	95.22 ± 0.01	96.06 ± 0.02
ϵ^*_{ID}	98.75 ± 0.01	99.10 ± 0.01	99.65 ± 0.01
$\epsilon^*_{\mathrm{ISO}}$	94.28 ± 0.01	94.25 ± 0.01	99.74 ± 0.01
$\epsilon^*_{\mathrm{TRK,SA,ID,ISO}}$	84.21 ± 0.02	88.22 ± 0.01	95.46 ± 0.02
$\epsilon^*_{\mathrm{HLTDoubleMu}}$	91.72 ± 0.01	94.19 ± 0.01	97.38 ± 0.01

response modelling between data and MC in p_{T} and η of the muons. Overall correction

maps per muon are given in 5.2.

After applying muon trigger and selection criteria together with correction factors, we select Z candidates and check the data to MC comparison illustrated in Figs. 5.3 and 5.4.

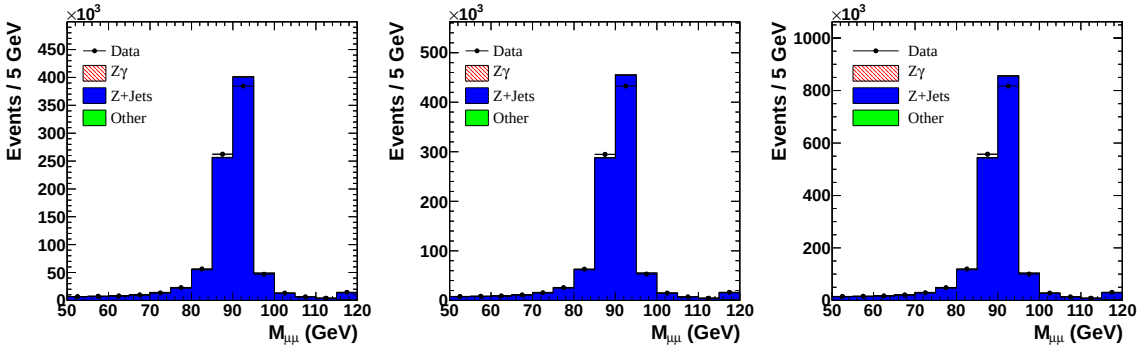

Figure 5.3: Z peak distribution in Z→ $\mu\mu$ without photon requirement for run A (left), run B (center), and combined (right).

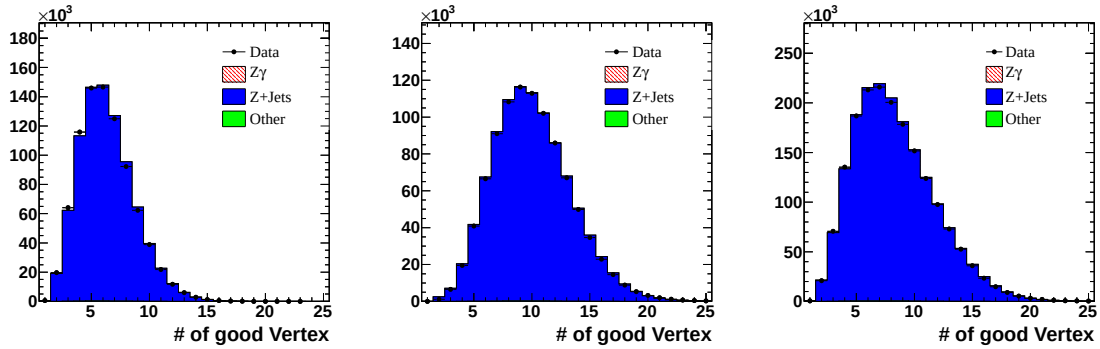

Figure 5.4: number of good vertices distribution in Z→ $\mu\mu$ without photon requirement for run A (left), run B (center), and combined (right).

5.4.2 Photon selection

Once we selected a Z candidate, we require a photon candidate to present in the event with $E_{\mathrm{T}}^{\gamma} > 15$ GeV and in the acceptance region of the ECAL detector. The efficiency of the photon to be reconstructed as SuperCluster (SC) is very close to 100%, thus we rely on MC simulation for its calculation. We apply further identification criteria to the photon candidates to reduce the background rate coming from "fake" objects that are mainly fragmentation objects from hadronic jets. The identification criterion is similar to one used in preceding 2010 analysis[30], except this time isolation variables also consider the energy contribution from the pile up:

- ECAL isolation $< 4.2 + 0.006 \times E_{\mathrm{T}}^{\gamma}$; this isolation variable is energy deposit in ECAL calorimeter within a hollow cone ($0.06 < R < 0.40$), excluding a rectangular strip of $\Delta\eta \times \Delta\phi = 0.04 \times 0.40$.
- HCAL isolation $< 2.2 + 0.0025\ E_{\mathrm{T}}^{\gamma}$,
- Hadronic/EM < 0.05,
- Hollow cone track isolation $< 2 + 0.001\ E_{\mathrm{T}}^{\gamma}$,
- $\sigma_{i\eta i\eta}(\eta\text{-width}) < 0.011$ (EB), < 0.030 (EE),
- Track veto: require no pixel seeds.

Photon isolation has a correction (ρ) due to pile up contribution :

$$\mathrm{Iso}^{\mathrm{new}} = \mathrm{Iso}^{\mathrm{original}} - \rho_{\mathrm{event}} \times A_{eff} \tag{5.3}$$

The energy density ρ_{event}, is the median background density per unit area and a measure of the pile-up activity in the event. A_{eff}, the effective area, is defined as the ratio of the slope obtained from linearly fitting $Iso(N_{vtx})$ to the one from linearly fitting $\rho_{\mathrm{event}}(N_{vtx})$. By applying this correction to isolation, the efficiency is made stable with respect to changing pile-up conditions.

Table 5.5: A_{eff} used for PU correction for photon selection for EB and EE, respectively.

Isolation	EB	EE
Tracker	0.0167	0.032
ECAL	0.183	0.090
HCAL	0.062	0.180

Comparison of corrected photon isolation variable shapes for data and MC simulation after applying full selection criteria is shown in Fig. 5.5. The results are in good agreement between data and MC simulation for all three isolation variables.

On the next step, we compare the photon performance (except pixel seed veto) in MC simulation and data using Tag and Probe technique with electrons from Z boson decay. The reason behind this is that we do not have a good source of high E_{T}^{γ}. As in the muon Tag and Probe, in this case we select electrons from Z boson decays, that are treated as photons. Events are selected with two photons requiring the invariant mass of the tag and probe pair to be consistent with the Z boson mass, *i.e.* within 50 and 150 GeV. Both tag and probe electrons must have hadronic over electromagnetic fraction less then 0.15, $E_{\mathrm{T}} > 20$ GeV, positioned in the ECAL fiducial region. We require photons to be matched to double electron triggers with one of the legs to be very loose. To avoid the bias, we specify Tag to be matched to tight leg of this trigger, and then test the selection criterion on the

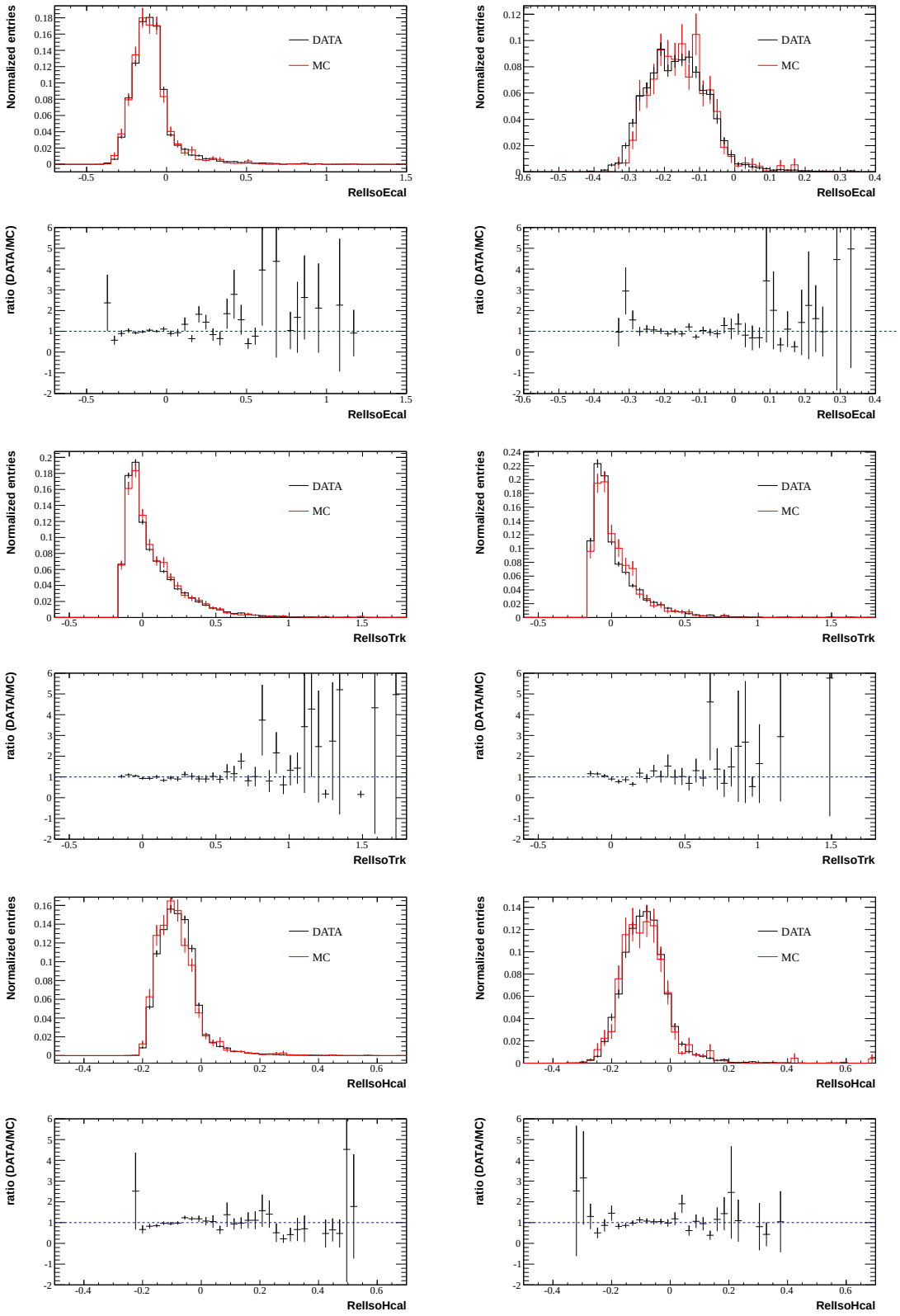

Figure 5.5: Pileup corrected photon isolation variables for barrel (left) and endcap (right)[2].

Table 5.6: photon identification scale factors

ECAL	Uncertainties				
	Scale factor	Fitting	Background shape modeling	Transverse energy binning	Total
Endcap-	1.038	0.006	0.005	0.039	0.040
Barrel	0.993	0.002	0.004	0.034	0.035
Endcap+	1.037	0.006	0.005	0.039	0.040

loose leg. The rest of the procedure follows the standards already described in previous section.

Similarly, to what we did with muon identification criteria, we calculate the corresponding scale factor to photon identification criteria with Tag and Probe tool, and overall correction maps are shown in Fig. 5.6

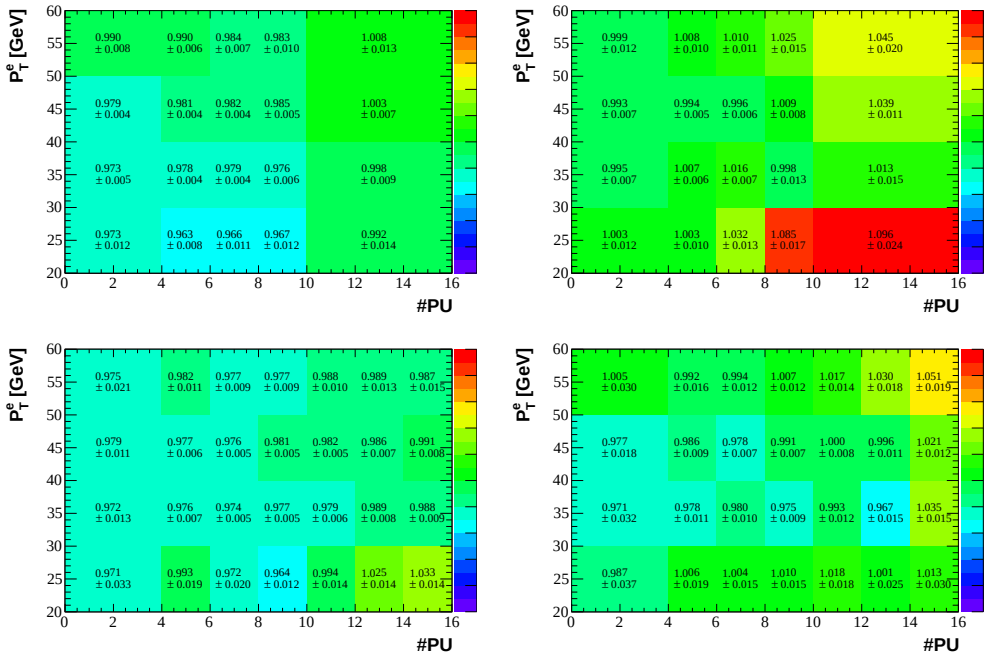

Figure 5.6: Scale factor for photon ID criteria for run A (top) and run B (bottom), Barrel (left) and Endcap (right).

5.5 Determination of backgrounds

We refer to the energy spread of the supercluster in the η direction as a shower shape variable, denoted as $\sigma_{i\eta i\eta}$. It is commonly used to separate the genuine photons from misidentified jets. Usually, unconverted photons deposit their energy in a narrow window in *eta*, but because of the mechanism how the jets fake photons (through mesons producing a pair

of photons), the $\sigma_{i\eta i\eta}$ for such objects is usually spread over the wider region, compared to genuine photons. The technique that utilizes this characteristic is called "Template" method. This method fits the $\sigma_{i\eta i\eta}$ distribution with the extended maximum likelihood two-component fit, with already predefined signal and background templates.

The signal component shape is obtained from MC and corrected for the difference between data and MC simulation in an electron control sample obtained from $Z \to ee$ events. This correction is small and is of the order of one percent. The background component shape was derived from data. The exact definition of $\sigma_{i\eta i\eta}$ variable is as followed:

$$\sigma^2_{i\eta i\eta} = \frac{\sum (\eta_i - \bar{\eta})^2 w_i}{\sum w_i}, \ \bar{\eta} = \frac{\sum \eta_i w_i}{\sum w_i}, \ w_i = \max(0, 4.7 + \log(E_i/E_{5\times5})), \tag{5.4}$$

where the sum runs over the 5×5 crystal matrix around the most energetic crystal in the SC.

Both signal and background templates are obtained seperately in bins of E^{γ}_{T}, also each devided seperately barrel ($\eta^{\mathrm{SC}} < 1.4442$) and endcap ($1.556 < |\eta^{\mathrm{SC}}| < 2.5$) region: $15 - 20$ GeV, $20 - 25$ GeV, $25 - 30$ GeV, $30 - 35$ GeV, $35 - 40$ GeV, $40 - 60$ GeV,$60 - 90$ GeV, and $90 - 500$ GeV.

5.5.1 Signal component shape

We used MadGraph MC simulator to obtain the $\sigma_{i\eta i\eta}$ shape of the signal. All difference in the modeling between data and MC, the disrtribution of $\sigma_{i\eta i\eta}$ was corrected by a scale factor, obtained from comparison of electron shower shapes using $Z \to ee$ events.

Fig. 5.7 illustrates the comparison of the $\sigma_{i\eta i\eta}$ distributions for the probe in data and simulation. The mean of the $\sigma_{i\eta i\eta}$ distribution in MC is bigger than that in data for both barrel and endcap. We correct this difference by shifting the shower shape distributions in simulation so that mean values are the same.

5.5.2 Background component shape

The background templates were obtained directly from the data, using a dataset containing high-purity jets. We select photon candidates in this sample requiring above-mentioned photon identification criteria, except the shower shape requirement. Additionally, the requirement on tracker isolation criteria $\mathrm{Iso}_{\mathrm{TRK}}$ is" inverted":

- $2 < \mathrm{Iso}_{\mathrm{TRK}} - 0.001 \cdot E^{\gamma}_{\mathrm{T}} - 0.0167 \cdot \rho < 5$ GeV for photons reconstructed in the barrel
- $2 < \mathrm{Iso}_{\mathrm{TRK}} - 0.001 \cdot E^{\gamma}_{\mathrm{T}} - 0.0320 \cdot \rho < 3$ GeV for photons reconstructed in the endcap

The idea behind inverting the tracker is isolation is to eliminate the contribution to the background templates from genuine isolated photons, that are produced together with jets. The $\sigma_{i\eta i\eta}$ distributions obtained from background simulation and data after applying the anti-track isolation requirement are given in Figs. 5.8.

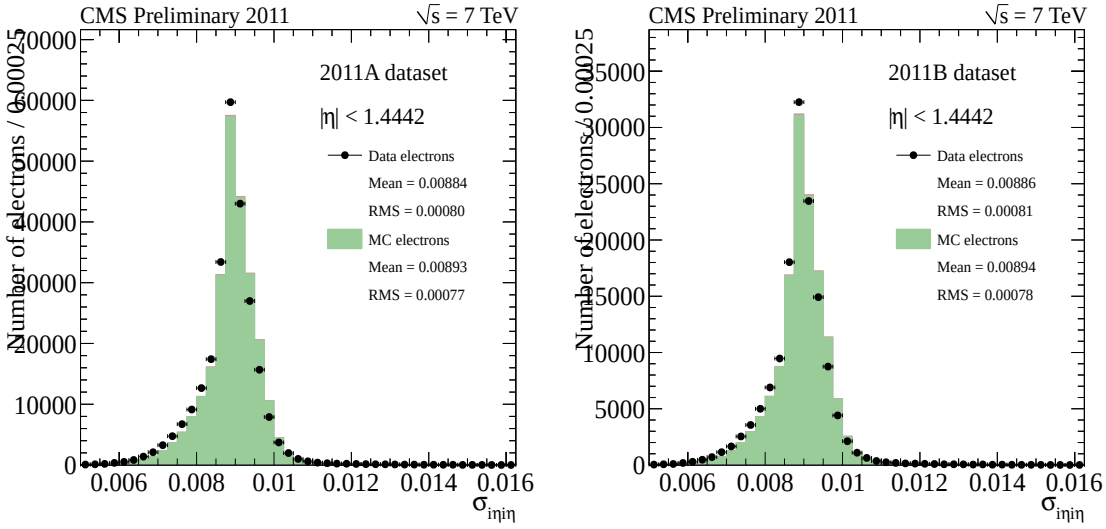

Figure 5.7: The $\sigma_{i\eta i\eta}$ distributions for run A (left) and run B (right). The difference of mean values between simulation (filled green histograms) and data (black dots) are accounted for by shifting the simulation signal shapes.

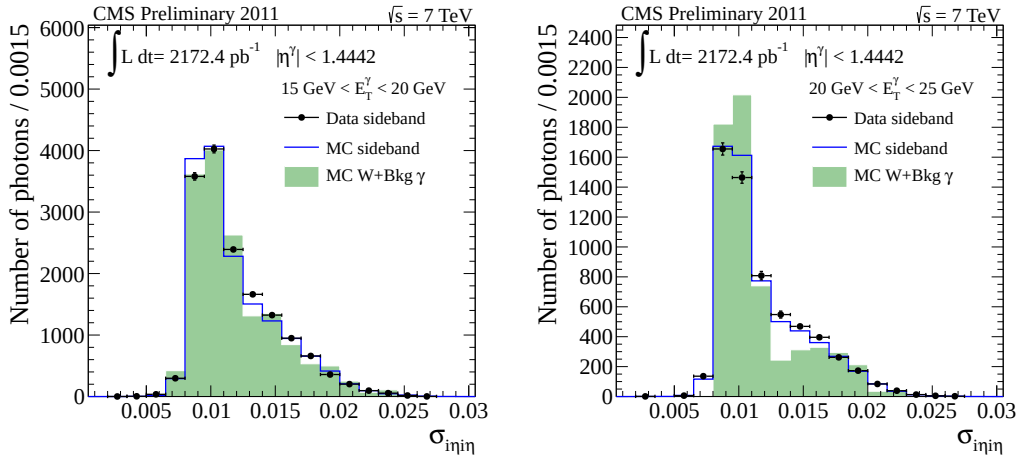

Figure 5.8: Z+Bkg photon (light green histogram) and estimated (blue line) background $\sigma_{i\eta i\eta}$ distributions from MC simulation and data (black dots) for each p_{T} bin in the barrel region. MC distributions are normalized to the same luminosity as the data sample[2].

5.5.3 Two-component fit

After we got the signal and background $\sigma_{i\eta i\eta}$ shape templates, we fit the shower shape distribution of photons in data with:

$$f(\sigma_{i\eta i\eta}) = \mathrm{N}_{\mathrm{signal}} \cdot S(\sigma_{i\eta i\eta}) + \mathrm{N}_{\mathrm{backgtround}} \cdot B(\sigma_{i\eta i\eta}), \tag{5.5}$$

where $\mathrm{N}_{\mathrm{signal}}$ and $\mathrm{N}_{\mathrm{backgtround}}$ are the estimated number of signal and background candidates, $S(\sigma_{i\eta i\eta})$ and $B(\sigma_{i\eta i\eta})$ are the signal and background component templates.

We utilize unbinned extended maximum likelihood fit, by minimizing:

$$\mathcal{L} = -\ln L = (\mathrm{N}_{\mathrm{signal}} + \mathrm{N}_{\mathrm{backgtround}}) - \sum_{i=1}^{n} N_i \ln(\mathrm{N}_{\mathrm{signal}} S_i + \mathrm{N}_{\mathrm{backgtround}} B_i). \tag{5.6}$$

where n is the number of bins in the $\sigma_{i\eta i\eta}$ distribution, N_i is the observed number of events for the i-th $\sigma_{i\eta i\eta}$ bin and S_i and B_i are the values of the corresponding components in that bin; N is the total number of data events in the given p_{T} bin.

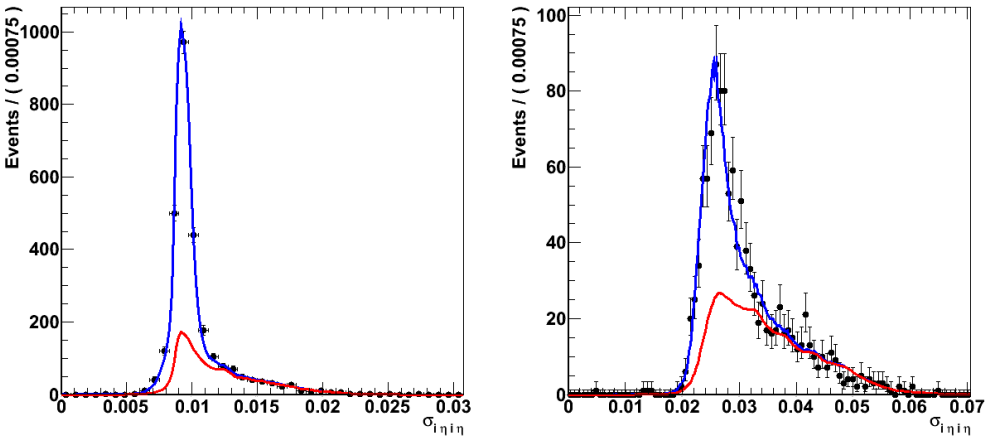

Figure 5.9: Template method fit example for the photon E_{T} bin 15-20 GeV in Barrel (left) and Endcap (right).

The result of the Template method is cross checked with another data-driven method, referred to as "Ratio" method, described in[2]. As illustrated in Fig. 5.15, background estimation results are consistent within uncertainty. We use results from Template method as a baseline for background estimation in this analysis.

5.6 Data/MC comparison

Once we apply full selection criteria; we compare the results from observed and expected (background from data plus MC) distributions. The data yields a total of 6463 candidates;

this agrees well with 6433.0 ± 101.8 expected events, with 5028.6 ± 36.4 of predicted $Z\gamma \to \mu\mu\gamma$ events and 1404.4 ± 95.1 of background events. The photon E_T, η, ϕ, dilepton and dilepton+photon invariant mass distributions for data with complete statistics (both run A and B) and MC simulations are shown in Fig. 5.10, Fig. 5.11. Pile up re-weighting for MC samples is applied in order to get the consistent pile up distribution shown in Fig. 5.12. Data and Data-driven background with MC signal agree well in all distributions. The comparison of fitted background yields between the individual runs and the full dataset is shown in Fig. 5.14.

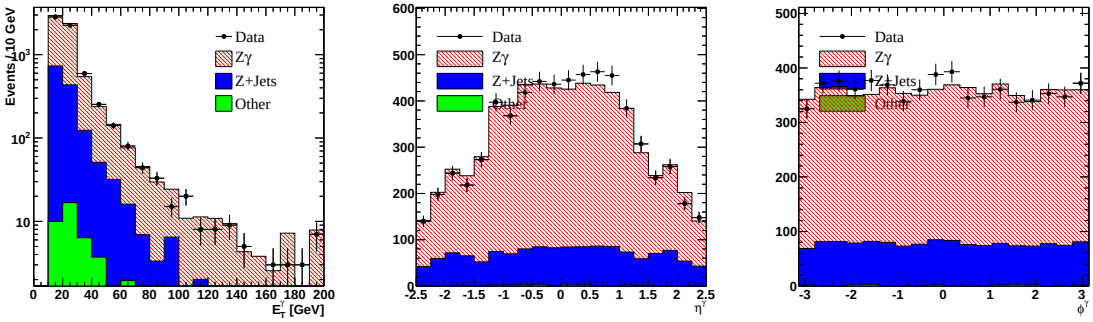

Figure 5.10: Distributions for the photon candidate E_T (left), η (center), and ϕ (right). Data (black dots), $Z\gamma$ signal (white histogram), Z/γ^*+jets and other backgrounds are given as red and green filled histograms respectively.

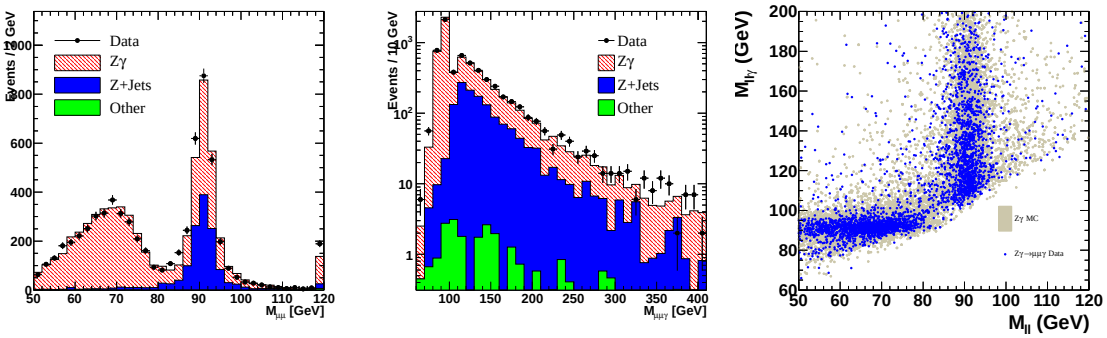

Figure 5.11: Dimuon mass distribution (left), Dimuon+photon mass (center), and 2 body versus 3 body mass (right).

The contributions from the backgrounds like QCD multijet, photon+jets, $t\bar{t}$, and other di-boson processes are very small (less than 1%), thus they are estimated from MC simulation and overall contribution passing final selection consists of 23.7 ± 2.2 events.

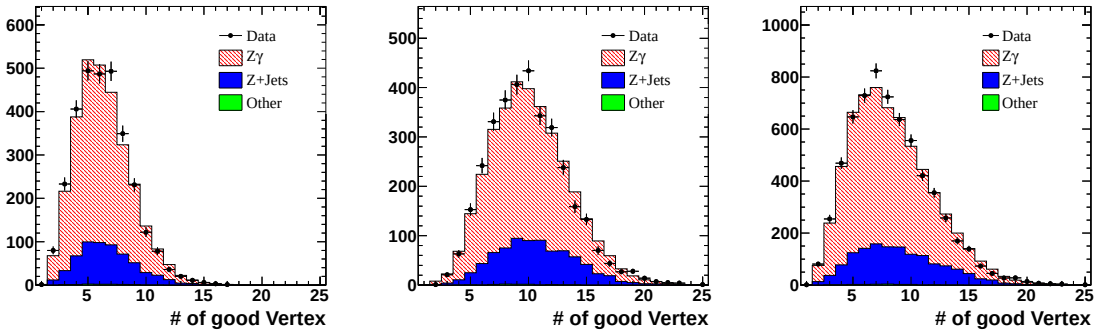

Figure 5.12: Number of vertices distribution after MC pile up re-weighting for run A (left), run B (cemter), and combined (right).

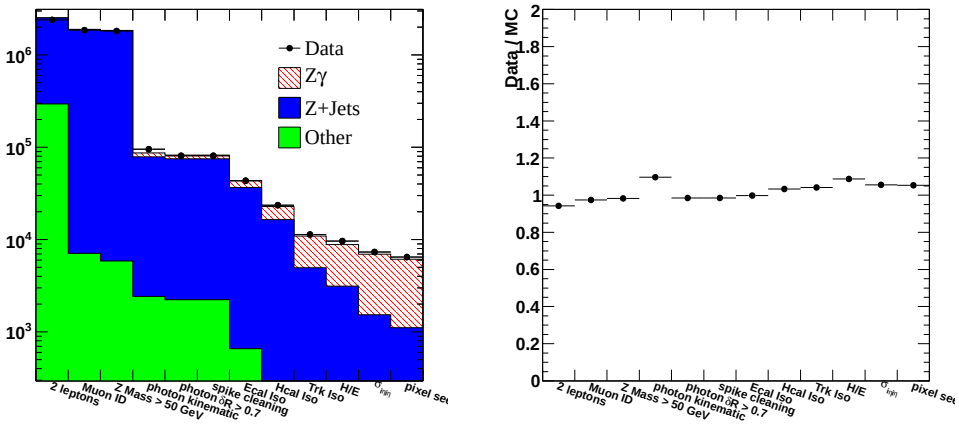

Figure 5.13: Event yields passing different cuts in data and MC (left) and their ratios (right).

Table 5.7: 2011A Z/γ^*+jets background estimation for the template method compared to MC truth(Z+jets only). The uncertainty for the data-driven method is statistical and systematic, while the MC truth uncertainty is statistical only.

ECAL	Template	MC truth
Barrel	368.7 ± 32.8 (stat.) ± 17.9 (syst.)	310.8 ± 10.8
Endcap	220.0 ± 19.9 (stat.) ± 12.4 (syst.)	165.7 ± 8.0
Total	588.7 ± 38.4 (stat.) ± 21.8 (syst.)	476.4 ± 13.4

5.7 Systematic uncertainties

The systematic uncertainties are assigned to the Zγ cross section measurement due to the following:

Table 5.8: 2011B Z/γ^*+jets background estimation for the template method compared to MC truth(Z+jets only). The uncertainty for the data-driven method is statistical and systematic, while the MC truth uncertainty is statistical only.

ECAL	Template	MC truth
Barrel	536.5 ± 37.0 (stat.) ± 27.8 (syst.)	383.8 ± 11.7
Endcap	257.7 ± 21.0 (stat.) ± 13.6 (syst.)	195.3 ± 8.5
Total	794.2 ± 42.5 (stat.) ± 31.0 (syst.)	579.1 ± 14.4

Table 5.9: Z/γ^*+jets background estimation for the template method compared to MC truth(Z+jets only) using full 2011 dataset. The uncertainty for the data-driven method is statistical and systematic, while the MC truth uncertainty is statistical only.

ECAL	Template	MC truth
Barrel	914.7 ± 63.2 (stat.) ± 110.2 (syst.)	383.8 ± 11.7
Endcap	489.6 ± 43.9 (stat.) ± 37.3 (syst.)	195.3 ± 8.5
Total	1404.3 ± 77.0 (stat.) ± 116.4 (syst.)	579.1 ± 14.4

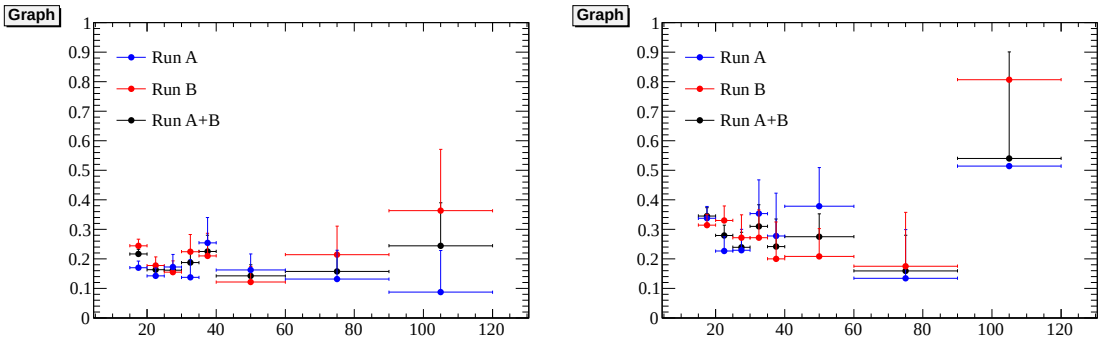

Figure 5.14: Background fraction in Barrel (left) and Endcap (right).

5.7.1 Luminosity

The CMS determine the total integrated luminosity, using so called pixel cluster counting technique[31]. For 2011 data the total systematic uncertainty on the luminosity is found to be 2.2% for the full dataset.

5.7.2 photon energy scales and resolution

Photon energy scale is one of the major sources of systematic uncertainty in this analysis. This is due to migration effect on the exponential shape of the photon p_{T} spectrum, migrating in and out of the acceptance region defined by E_{T}^{γ} cut. To estimate the overall effect, we vary the photon energy scale by 1% in Barrel and 3% in Endcap. W also smear the reconstructed photon energy in simulation to match that one in data. As a result, the $A \cdot \varepsilon_{MC}$

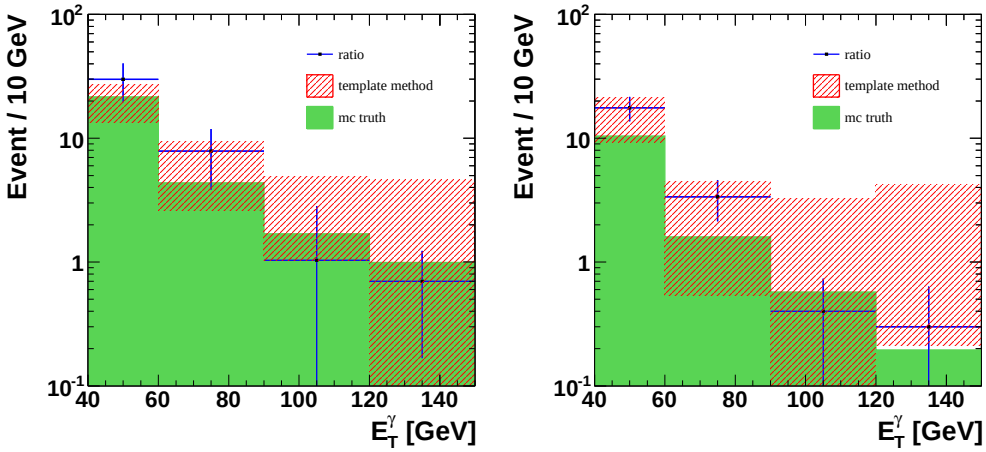

Figure 5.15: Estimated background comparison between Template and Ratio method for the Barrel (left) and Endcap (right).

varies with energy scale and resolution. To estimate the systematic effect on the measured cross section the number of signal events is recalculated for each systematic variation, including the effects on data-driven background predictions. Finally, the difference between each variation and the nominal cross section value is assigned as systematic uncertainty.

5.7.3 Pileup

MC pileup distribution is normalized to data pileup distribution, thus we shift the data distribution by $\pm 5\%$ that corresponds to the inelastic pp scattering cross section error. Accordingly, MC signal sample is re-normalized to these new data pileup distributions, and $A \cdot \varepsilon_{MC}$ is recalculated.

5.7.4 PDF

The acceptance also depends on the choice of Parton Density Function (PDF), chosen within the simulation. The systematic uncertainty from the PDF is estimated by varying the PDF re-weighing methods within different PDF sets, that were used in MC generation. We are using CTEQ6L[32] PDF libraries and the "modified tolerance method" to estimate the uncertainty due to the PDF. The largest deviation from the nominal cross section is assigned as the systematic uncertainty on PDF.

5.7.5 Data/MC correction factors

The lepton/photon performance study with tag and probe depends on the modeling choices of the signal and background, as well as the statistics of the samples. We calculate the systematic uncertainty on the muon and photon scale factor by varying the modeling function

for signal and background shapes. Additionally, tag and probe can measure the efficiencies up to some precision, which is determined from the comparison of photon efficiency using Monte Carlo level information, and the tang and probe results on the same sample. These effects are propagated to acceptance, and the maximum deviation from the nominal value is assigned as uncertainty.

5.7.6 Background estimation with Template method

Another major source of systematic uncertainty on cross section measurement is coming from the Template method, which is further divided into following:

1. Signal shape: As we mentioned in Section 5.5.1, signal component shapes of $\sigma_{i\eta i\eta}$ are obtained from simulation, and a shift correction is then applied to them. The systematic uncertainty on signal shape is calculated as the difference on a background yield using shapes with and without shift correction.

2. Background shape: Because the background component shape was taken from the data with a different dataset, the $\sigma_{i\eta i\eta}$ distribution from this sample doesn't necessarily represent the exact shape in the signal region. Thus, we rely on MC simulation to account for shape variation. Additionally, part of this shape is contaminated by the genuine photons, the effects of which is also estimated from MC simulation. The uncertainties related to background $\sigma_{i\eta i\eta}$ shapes are shown in Figs. 5.16.

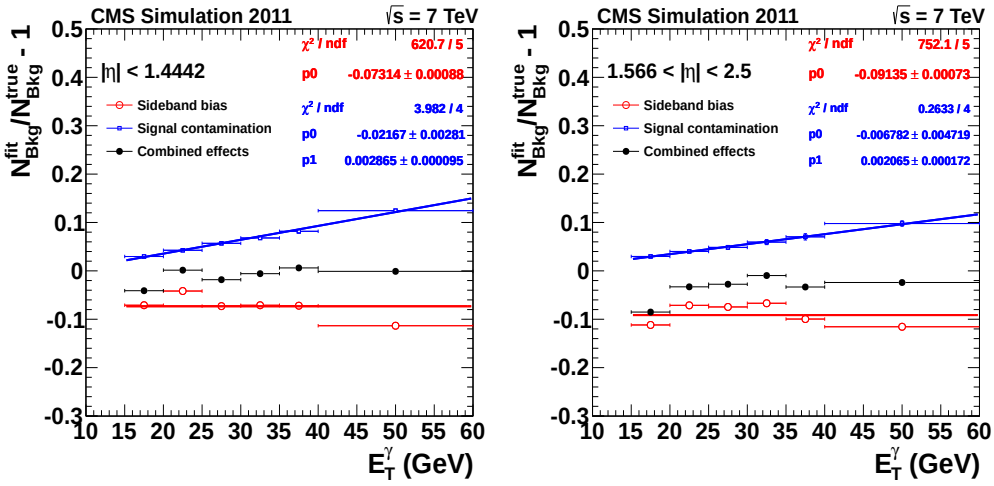

Figure 5.16: The uncertainty on the background template for barrel (left) and endcap (right) is illustrated. The uncertainty due to sideband bias is labeled as red dots. The uncertainty due to signal contamination is labeled as blue dots[2].

5.8 Measurement of the Zγ cross section

The cross section is calculated with the following formula:

$$\sigma_{Z\gamma\to ll\gamma} = \frac{\mathrm{N}_{\mathrm{observed}} - N_{\mathrm{background}}}{A \cdot \epsilon_{MC,\mathrm{Z}\gamma\to ll\gamma} \cdot \rho_{eff} \cdot \int \mathcal{L}\, dt}, \tag{5.7}$$

Where $\mathrm{N}_{\mathrm{observed}}$ is the number of observed Zγ candidates after the full selection, $N_{\mathrm{background}}$ is the estimated number of background events, and where $N_{\mathrm{background}} = \mathrm{N}^{DataDriven}_{\mathrm{backgtround}} + \mathrm{N}^{other}_{\mathrm{backgtround}}$, $\mathrm{N}^{DataDriven}_{\mathrm{backgtround}}$ is the number of fake photons from jets estimated from template method, and $\mathrm{N}^{other}_{\mathrm{backgtround}}$ is the number of other sources estimated by MC. A is the signal acceptance, and $\epsilon_{MC,\mathrm{Z}\gamma\to ll\gamma}$ is the efficiency for all requirements of the event selection. The $A \cdot \epsilon$ is defined as $N_{\mathrm{accept}}/N_{gen,\ kin}$, where the N_{accept} is the number of events passing all selection cuts, and the $N_{gen,\ kin}$ is the number of generated events with $E^{\gamma}_{\mathrm{T}} > 15$ GeV, $\Delta R_{\ell,\gamma} > 0.7$ and $M_{\ell\ell} > 50$ GeV. The $\int \mathcal{L}\, dt$ is the integrated luminosity, and ρ_{eff} is a correction factor that takes into account the data/simulation efficiency differences. The ρ_{eff} is calculated as a product of data/MC correction factors for muon and photon reconstruction and identification.

The numbers that are used to calculate the cross sections are summarized in tables 5.10, 5.11, and 5.12 for each run period. The estimated cross section of $\mathrm{Z}\gamma \to \mu\mu\gamma$ is $5.51 \pm 0.14(\mathrm{stat.}) \pm 0.29(\mathrm{syst.}) \pm 0.12(\mathrm{lumi.})$ pb. for run A, $5.40 \pm 0.13(\mathrm{stat.}) \pm 0.28(\mathrm{syst.}) \pm 0.12(\mathrm{lumi.})$ pb. for run B and $5.43 \pm 0.10(\mathrm{stat.}) \pm 0.29(\mathrm{syst.}) \pm 0.12(\mathrm{lumi.})$ pb. for full 2011 dataset.

The plot illustrating cross section measurement is shown in Figs. 5.17.

Table 5.10: Summary of parameters for the Zγ cross section measurement for run A.

$N_{observed}$	3047 ± 55.2 (stat.)
$\mathrm{N}^{DataDriven}_{\mathrm{backgtround}}$	588.7 ± 38.4 (stat.) ± 21.8 (syst.)
$\mathrm{N}^{other}_{\mathrm{backgtround}}$	12.1 ± 1.6 (stat.)
N_{Sig}	2446.1 ± 67.3 (stat.) ± 105.2 (syst.)
$A \cdot \epsilon_{MC}$	0.202 ± 0.001 (stat.)
ρ_{eff}	0.960 ± 0.016 (syst.)
$\int \mathcal{L}\, dt$	2289.9 ± 50.4 (syst.)

Table 5.11: Summary of parameters for the Zγ cross section measurement for run B.

$N_{observed}$	3416 ± 58.4 (stat.)
$N^{DataDriven}_{backgtround}$	794.2 ± 42.5 (stat.) ± 31.0 (syst.)
$N^{other}_{backgtround}$	11.6 ± 1.4 (stat.)
N_{Sig}	2610.1 ± 72.3 (stat.) ± 113.2 (syst.)
$A \cdot \epsilon_{MC}$	0.191 ± 0.001 (stat.)
ρ_{eff}	0.932 ± 0.016 (syst.)
$\int \mathcal{L}\ dt$	2709.0 ± 59.6 (syst.)

Table 5.12: Summary of parameters for the Zγ cross section measurement for full 2011 datasest.

$N_{observed}$	6463 ± 80.4 (stat.)
$N^{DataDriven}_{backgtround}$	1404.3 ± 56.4 (stat.) ± 77.0 (syst.)
$N^{other}_{backgtround}$	23.7 ± 2.2 (stat.)
N_{Sig}	5034.9 ± 98.2 (stat.) ± 213.2 (syst.)
$A \cdot \epsilon_{MC}$	0.196 ± 0.001 (stat.)
ρ_{eff}	0.945 ± 0.016 (syst.)
$\int \mathcal{L}\ dt$	4998.9 ± 110.0 (syst.)

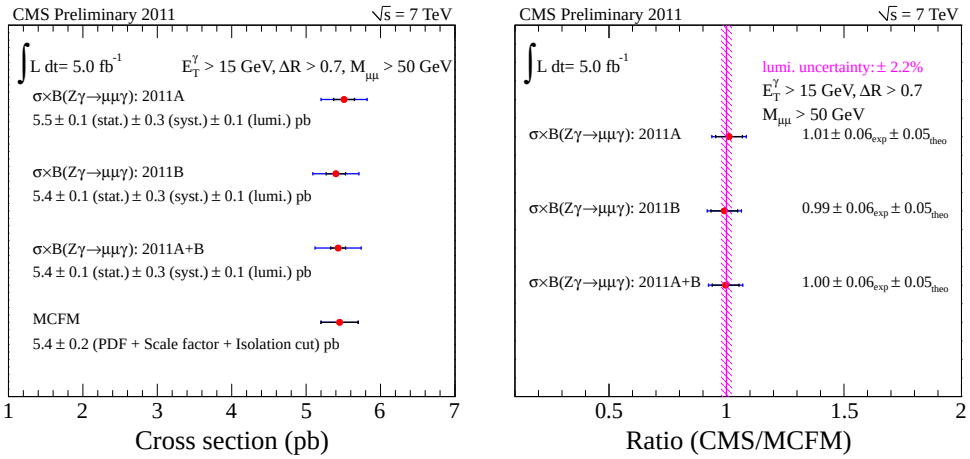

Figure 5.17: The cross section of Zγ in muon channel measured using 2011A, 2011B and full 2011 datasets and MCFM prediction (left), and ratio between measured cross section to the MCFM prediction (right).

Table 5.13: Summary of systematic uncertainties for the Zγ cross section measurement for 2011A dataset.

		$ee\gamma$	$\mu\mu\gamma$
Source	Systematic uncertainty	Effect on N_{signal}	
Electron and photon energy scale	ele: 0.5%; pho: 1% (EB) 3% (EE)	2.5 %	n/a
Photon energy scale	1% (EB) 3% (EE)	n/a	4.25%
Muon p_T scale	0.2%	n/a	0.63%
Total uncertainty on N_{signal}		2.5 %	4.30%
Source	Systematic uncertainty	Effect on $\mathcal{F} = A \cdot \epsilon_{MC}$	
Electron and photon energy resolution		0.2 %	n/a
Photon energy resolution		n/a %	0.10%
Muon p_T resolution	0.6%	n/a	0.07%
Pileup	Shift data PU distribution by $\pm$ 5%	0.4 %	0.26%
PDF	CTEQ6L re-weighting	1.1 %	1.10%
Signal Modeling		0.6 %	1.10%
Total uncertainty on $\mathcal{F} = A \cdot \epsilon_{MC}$		1.3 %	1.14%
Source	Systematic uncertainty	Effect on ρ_{eff}	
Electron reconstruction	0.4%	0.8 %	n/a
Electron trigger	0.1%	0.1 %	n/a
Electron ID and isolation	2.3%	4.6 %	n/a
Muon trigger	1.5%	n/a	1.0 %
Muon reconstruction	0.9%	n/a	1.0 %
Muon ID and isolation	0.9%	n/a	1.8 %
Photon ID and isolation	0.5% (EB), 1.0% (EE)	0.5 %	1.00%
Total uncertainty on ρ_{eff}		4.7 %	2.51%
Source	Systematic uncertainty	Effect on background yield	
Template method	5.1% (EB), 13.7% (EE)	5.9 %	n/a
	2.2% (EB), 4.1% (EE)	n/a	3.7%
Total uncertainty on background		5.9 %	3.7%
Source	Systematic uncertainty	Effect on luminosity	
Luminosity	2.2%	2.2%	2.2%

Table 5.14: Summary of systematic uncertainties for the Zγ cross section measurement for 2011B dataset.

		$ee\gamma$	$\mu\mu\gamma$
Source	Systematic uncertainty	Effect on N_{signal}	
Electron and photon energy scale	ele: 0.5%; pho: 1% (EB) 3% (EE)	3.6 %	n/a
Photon energy scale	1% (EB) 3% (EE)	n/a	4.25%
Muon p_T scale	0.2%	n/a	0.87%
Total uncertainty on N_{signal}		3.6 %	4.34%
Source	Systematic uncertainty	Effect on $\mathcal{F} = A \cdot \epsilon_{MC}$	
Electron and photon energy resolution	1% (EB), 3% (EE)	0.2 %	n/a
Photon energy resolution	1% (EB), 3% (EE)	n/a	0.03%
Muon p_T resolution	0.6%	n/a	0.10%
Pileup	Shift data PU distribution by $\pm$ 5%	0.6 %	0.61%
PDF	CTEQ6L re-weighting	1.1%	1.10%
Signal Modeling		0.6 %	1.10%
Total uncertainty on $\mathcal{F} = A \cdot \epsilon_{MC}$		1.4 %	1.29%
Source	Systematic uncertainty	Effect on ρ_{eff}	
Electron reconstruction	0.4%	0.8 %	n/a
Electron trigger	0.1%	0.1 %	n/a
Electron ID and isolation	2.5%	5.0 %	n/a
Muon trigger	1.5%	n/a	1.0 %
Muon reconstruction	0.9%	n/a	1.0 %
Muon ID and isolation	0.9%	n/a	2.30%
Photon ID and isolation	0.5% (EB), 1.0% (EE)	0.5 %	1.00%
Total uncertainty on ρ_{eff}		5.1 %	2.51%
Source	Systematic uncertainty	Effect on background yield	
Template method	6.3% (EB), 7.4% (EE)	4.9 %	n/a
	4.9% (EB), 5.8% (EE)	n/a	3.9%
Total uncertainty on background		4.1 %	3.9%
Source	Systematic uncertainty	Effect on luminosity	
Luminosity	2.2%	2.2%	2.2%

Table 5.15: Summary of systematic uncertainties for the Zγ cross section measurement for full 2011 dataset.

		$\mu\mu\gamma$
Source	Systematic uncertainty	Effect on N_{signal}
Photon energy scale	2%	4.19%
Muon p_T scale	0.2%	0.60%
Total uncertainty on N_{signal}		4.23%
Source	Systematic uncertainty	Effect on $\mathcal{F} = A \cdot \epsilon_{MC}$
Photon energy resolution	1% (EB), 3% (EE)	0.06%
Muon p_T resolution	0.6%	0.08%
Pileup	Shift data PU distribution by $\pm$ 5%	0.44%
PDF	CTEQ6L re-weighting	1.10%
Signal Modeling		1.10%
Total uncertainty on $\mathcal{F} = A \cdot \epsilon_{MC}$		1.22%
Source	Systematic uncertainty	Effect on ρ_{eff}
Muon trigger	1.5%	1.0 %
Muon reconstruction	0.9%	1.0 %
Muon ID and isolation	0.9%	2.30%
Photon ID and isolation	0.5% (EB), 1.0% (EE)	1.00%
Total uncertainty on ρ_{eff}		2.51%
Source	Systematic uncertainty	Effect on background yield
Template method	4.9% (EB), 5.8% (EE)	5.5%
Total uncertainty on background		5.5%
Source	Systematic uncertainty	Effect on luminosity
Luminosity	2.2%	2.2%

Chapter 6

Anomalous trilinear Gauge couplings

As described in 2.2.1, a measurement of anomalous Trilinear Gauge Coupling (TGC) is important as it is sensitive to new phenomena. In this chapter, we describe the measurements of the ZZγ, and Z$\gamma\gamma$ couplings at $\sqrt{\hat{s}} = 7$ TeV.

6.1 Monte Carlo modelling and NLO effects with tgc

We generate aTGC signal using SHERPA generator interfaced with PYTHIA[33] for the detector simulation of the Zγ+n jet (n $\leq$ 1) process. Two aTGC parameters, h_3^{V} and h_4^{V} with V = Z, γ are freely varied. Note that this is leading order generator, thus it is important to take into account corrections coming from processes QED and QCD. The corrections on the couplings due to the QED processes are very small[19], therefore, neglected. However, the correction coming from QCD are can be as big as the factor of two or even three depending on the experimental environment, as a result it is crucial to consider correction coming from next to leading processes (NLO). Figure 6.1 illustrates the amount of NLO corrections for various anomalous trilinear coupling points - the larger the coupling the smaller the NLO correction effect is. Thereby, when setting limits on anomalous couplings, we include additional systematic uncertainty on photon E_{T} spectrum due to NLO corrections. Consequently, in this study, for the SM sample, where aTGC is set to 0, a p_{T}-dependent $k-$factor is used. Furthermore, we estimate the overall effect due to aTGC k-factors to be well within 10%, which is taken into account by assigning additional systematic uncertainty on the NLO signal modeling when setting the limits.

6.2 aTGC observable

The inclusion of the anomalous coupling parameters in the SM Lagrangian results in the enhanced differential cross-section of di-boson production at large $\hat{s}$. This means with aTGC an excess of events occurs on high momentum of bosons. For Zγ production this is easily observed in photon p_{T}. Direct access to the photon, distinguishes this channel with its sensitivity compared to di-boson process without a photon (i.e. WW, ZZ or WZ). We

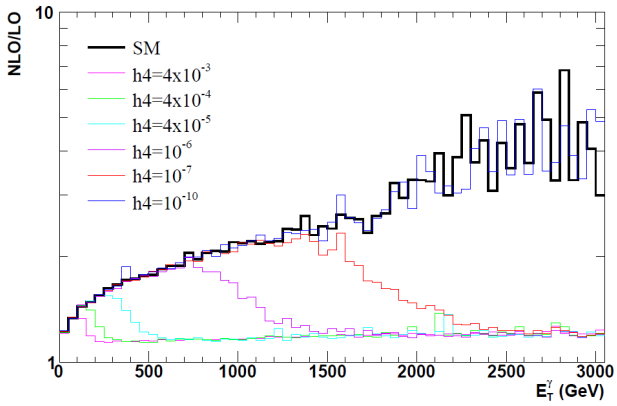

Figure 6.1: Effects of NLO correction as a function of aTGC.

use photon E_{T} as the observable to measure aTGCs. The aTGC results are interpreted by setting the limits on the ratio of the observed signal to that of the expected aTGC yield, using the likelihood formalism. The statistical tool, used in the limit setting is called CLs method[34].

6.2.1 aTGC normalization

The presence of the aTGC violates the partial wave unitarity at high energies[35]. To preserve unitarity, dependence of the amplitude of anomalous coupling on $\hat{s}$ was introduced:

$$\alpha(\hat{s}) = \frac{\alpha_0}{(1+\hat{s}/\Lambda_{NP}^2)^n}. \tag{6.1}$$

Where, α_0 is a low-energy approximation of the coupling $\alpha(\hat{s})$, $\hat{s}$ is the square of the invariant mass of the diboson system, and Λ_{NP} is the form factor scale, an energy at which new physics become non negligible. Due to the assumption on the form of the energy dependence, we do not consider this factorization in this study.

6.2.2 Setting the limits on aTGC in Zγ production

The data agrees with the SM prediction with no anomalous trilinear gauge couplings, thus we set the limits on aTGC parameters h_3^{V}, and h_4^{V} . The photon E_{T} distribution of data and MC simulation is given in Fig. 6.2. The 95% confidense level (C.L.) two-dimensional contours are shown in 6.4 and 6.3 with no form-factors on the aTGC scenario. Their corresponding one-dimensional limits are presented in Table 6.1.

Coupling	h_3 Lower limit 10^{-3}	h_3 Upper Limit 10^{-3}	h_4 Lower limit 10^{-5}	h_4 Upper Limit 10^{-5}
$Z\gamma\gamma$	-13	13	-11	12
$ZZ\gamma$	-11	11	-10	11

Table 6.1: One-dimensional limits on $Z\gamma$ anomalous trilinear gauge couplings.

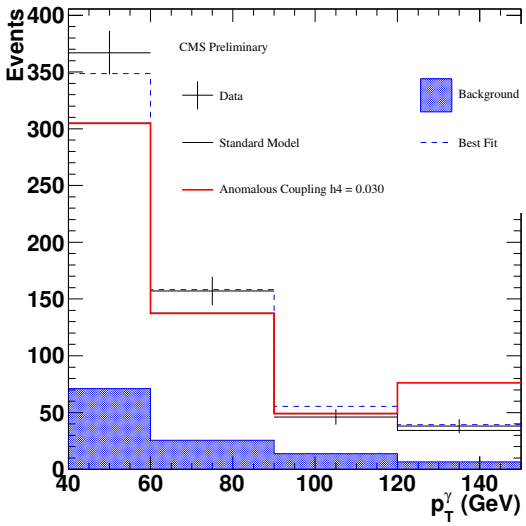

Figure 6.2: Photon E_{T} distribution for data (black circles), Z+jets background (blue filled histogram), SM signal (black histogram), and signal with one of aTGC points (red histogram). The last bin includes overflows.

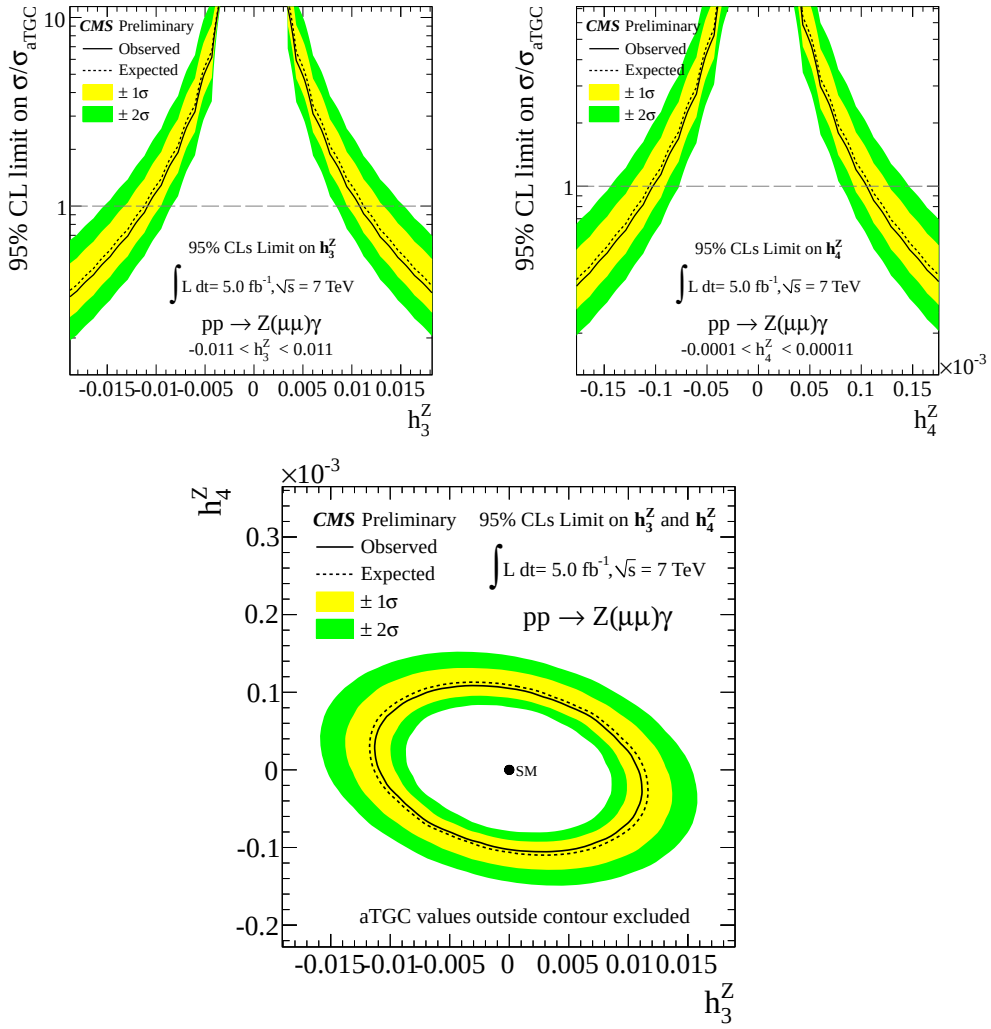

Figure 6.3: One-dimensional 95% confidence level limits on h_3^Z (left) and h_4^Z (right), followed by 2 Dimensional 95% confidence level limits for h_3^Z and h_4^Z (bottom).

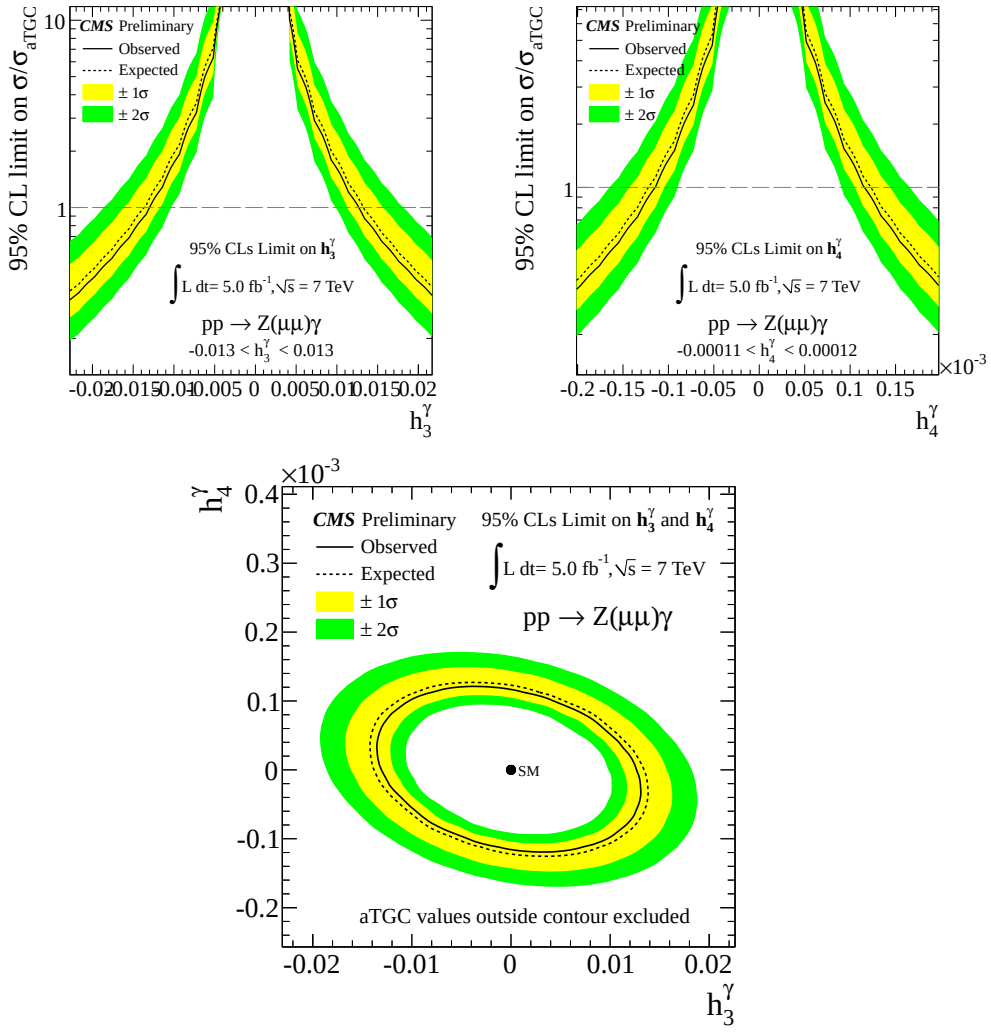

Figure 6.4: One-dimensional 95% confidence level limits on h_3^γ (left) and h_4^γ (right), followed by 2 Dimensional 95% confidence level limits for h_3^γ and h_4^γ (bottom).

Chapter 7

Search For Technicolor

Here, I present only the results on the sensitivity study on one of the channels in Technicolor production, described in section 2.2.2. The details of this analysis can be found in private note[3], available upon request.

This study focuses on the tri-lepton final state resulting from the ρ_T and a_T decay via a WZ pair ($\rho_T/a_T \to WZ \to \ell\ell\nu$). The ρ_T (and a_T) production in pp collisions at the LHC occur primarily through quark annihilation into an intermediate W^* boson. We concentrate on the signal with four TCSM mass points of ρ_T (225 GeV, 300 GeV, 400 GeV, and 500 GeV), that have not been previously excluded by other experiments. The discovery or exclusion of these masses is covered with less than ~ 10 fb^{-1}of integrated luminosity at $\sqrt{s} = 10$ TeV. The background MC samples generated for this study consist of $WZ \to lll\nu$, $ZZ \to llll$, $t\bar{t}$, Z+jets, QCD, and W+jets. All samples were generated with PYTHIA generator and are weighted to corresponding NLO cross sections. The analysis uses the standardized packages of mc generator, CMS detector simulation, together with object identification algorithms, and various data-driven background estimation techniques. The resulting reconstructed WZ invariant mass distribution is illustrated in the Figure 7.1.

7.1 Results

In the absence of an observed excess above background, we set a 95% C.L. upper limit on the cross-section. This 95% C.L. upper limit is calculated using a Bayesian statistical approach, assuming Poisson statistics. The limits are shown in Fig. 7.2 as a function of integrated luminosity. The horizontal lines indicate the theoretical cross section plus and minus 27% of theoretical uncertainty. The results are summarized in Table 7.1.

With a certain number of signal and background events at a particular luminosity, we calculate the significance by computing the probability for the background to fluctuate to or above the observed number of events. The discovery potential is evaluated for different luminosity settings. Figure 7.3 show the significance as a function of integrated luminosity for the four different parameter sets of ρ_T.

As a result, we find that it is feasible to exclude at 95% C.L. the $\rho_T \to WZ$ process for

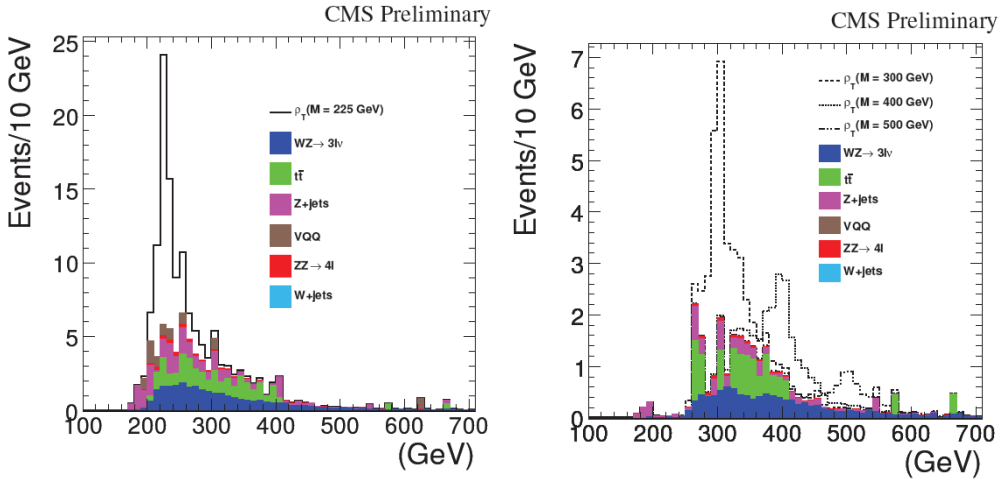

Figure 7.1: WZ invariant mass distributions for signal and background samples. ρ_T with mass 225 GeV on left and 300 GeV and more on right. The distributions are normalized to an integrated luminosity of 1 fb^{-1} [3].

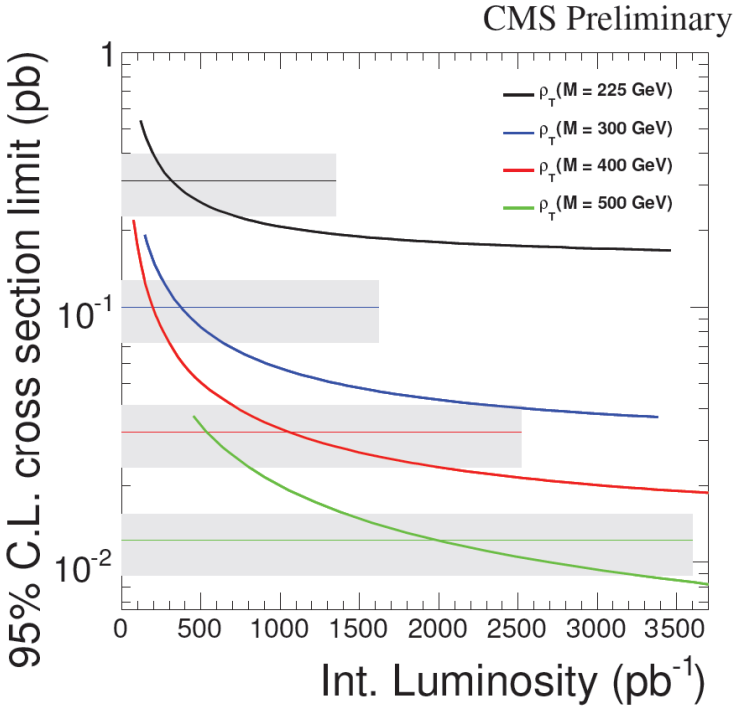

Figure 7.2: 95% C.L. limit for ρ_T as a function of integrated luminosity. The cross sections include the branching ratio to electrons and muons. The horizontal lines, which indicate the theoretical cross section (plus and minus its associated 27% uncertainty) [3].

Table 7.1: Integrated luminosity needed for cross section exclusion at 95% C.L., 3σ evidence, and 5σ discovery for different mass points.

Sample	Int. luminosity for 95% C.L. limit [(+, −) theoretical uncertainty] (pb^{-1})	Int. Luminosity for 3σ evidence (pb^{-1})	Int. Luminosity for 5σ evidence (pb^{-1})
ρ_T (M=225 GeV)	313(201, 625)	314	2808
ρ_T (M=300 GeV)	366(261, 645)	517	2264
ρ_T (M=400 GeV)	1052(701, 1981)	1775	> 4000
ρ_T (M=500 GeV)	2023(1397, 3256)	2380	> 4000

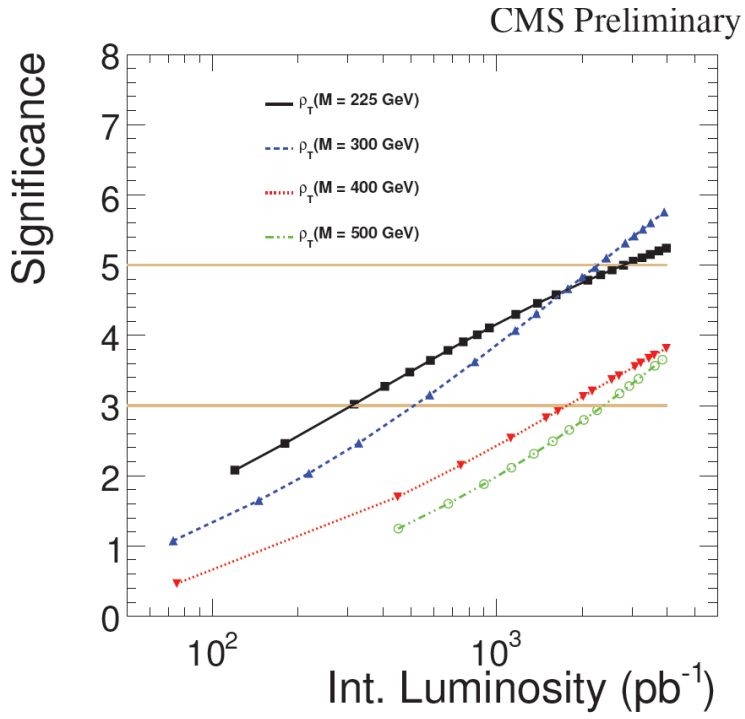

Figure 7.3: Significance as a function of integrated luminosity for ρ_T for different mass points[3].

ρ_T masses up to 400 GeV with $\sim$ 366 $pb^{-1}$of data. A 5σ observation of this process for these masses would need $\sim$ 2.8 $fb^{-1}$of data.

Chapter 8

Summary

I presented a detailed study of $Z\gamma \to \mu\mu\gamma$ production cross section measurement and set limits on anomalous trilinear gauge couplings with CMS detector using data with the total integrated luminosity of $\mathcal{L}$= 5 fb^{-1} , at the center of mass energy $\sqrt{s} = 7$ TeV. The observed kinematic parameters of the $Z\gamma \to \mu\mu\gamma$ production agrees well with the SM prediction. The measured cross-section is found to be $5.43 \pm 0.10(\text{stat.}) \pm 0.29(\text{syst.}) \pm 0.12(\text{lumi.})$ pb, while the SM prediction is 5.45 ± 0.27 pb. The uncertainties in the cross section measurement are comparable with theoretical - the main source is from the uncertainty in the photon energy scale and background estimation. The 95% confidence level limits on the aTGC corresponds to: $|h_3^\gamma| < 0.013$, $|h_4^\gamma| < 0.00012$, $|h_3^Z| < 0.011$ and $|h_4^Z| < 0.00011$.

As of today, the LHC delivered $\mathcal{L}$= 23 fb^{-1} of data at $\sqrt{s} = 8$ TeV, out of which $\mathcal{L}$= 21 fb^{-1} is recorded by the CMS and available for further analysis. The increase in the center of mass energy will tremendously improve the sensitivity to the new physics, allowing either observing significant deviation from the SM prediction, or resulting in tighter aTGC limits. Additionally, analysis will benefit from four times bigger statistics, compared to 2011 data. This will provide the opportunity for better background estimation techniques on high p_T spectrum of the photon, or possibly allowing access to the observable with greater sensitivity on aTGC.

In summary, the methods outlined in this thesis can be further applied for future searches for new phenomena and precision measurements of the trilinear and quartic couplings in the future analysis of data from LHC and other colliders.

Bibliography

[1] A. Purcell, "Go on a particle quest at the first cern webfest. le premier webfest du cern se lance la conqute des particules," p. 10, Aug 2012.

[2] "Study of Wγ and Zγ production at CMS with $\sqrt{s} = 7$ TeV ," *CMS Analysis Note*, vol. AN-2011-251, 2011.

[3] "Search for Technicolor with the CMS Experiment," *CMS Analysis Note*, vol. AN-2009-099, 2009.

[4] S. Dittmaier, S. Dittmaier, C. Mariotti, G. Passarino, R. Tanaka, *et al.*, "Handbook of LHC Higgs Cross Sections: 2. Differential Distributions," 2012.

[5] J. Berryhill, "CMS Standard Model Physics Results." https://twiki.cern.ch/twiki/bin/view/CMSPublic/PhysicsResultsSMP. Browsed on 2013-05-09.

[6] C. Lefvre, "The cern accelerator complex. complexe des acclrateurs du cern." Dec 2008.

[7] C. Collaboration, "Detector drawings." CMS Collection., Mar 2012.

[8] M. Herrero, "The Standard model," 1998.

[9] e. Evans, Lyndon and e. Bryant, Philip, "LHC Machine," *JINST*, vol. 3, p. S08001, 2008.

[10] S. Chatrchyan *et al.*, "The CMS experiment at the CERN LHC," *JINST*, vol. 3, p. S08004, 2008.

[11] G. Aad *et al.*, "The ATLAS Experiment at the CERN Large Hadron Collider," *JINST*, vol. 3, p. S08003, 2008.

[12] S. Chatrchyan *et al.*, "Observation of a new boson at a mass of 125 GeV with the CMS experiment at the LHC," *Phys.Lett.*, vol. B716, pp. 30–61, 2012.

[13] G. Aad *et al.*, "Observation of a new particle in the search for the Standard Model Higgs boson with the ATLAS detector at the LHC," *Phys.Lett.*, vol. B716, pp. 1–29, 2012.

[14] A. Pich, "Quantum chromodynamics," 1995.

[15] A. Azatov and J. Galloway, "Electroweak Symmetry Breaking and the Higgs Boson: Confronting Theories at Colliders," *Int.J.Mod.Phys.*, vol. A28, p. 1330004, 2013.

[16] T. L. Barklow, S. Dawson, H. E. Haber, and J. L. Siegrist, "Electroweak symmetry breaking and beyond the standard model," 1995.

[17] J. Andersen, O. Antipin, G. Azuelos, L. Del Debbio, E. Del Nobile, *et al.*, "Discovering Technicolor," *Eur.Phys.J.Plus*, vol. 126, p. 81, 2011.

[18] J. Han, "W and Z Boson Cross Section and W Asymmetry at CMS," 2011.

[19] U. Baur and E. Berger, "Probing the weak-boson sector in $Z\gamma$ production at hadron colliders," *Phys. Rev.*, vol. D47, p. 4889, 1993.

[20] C. Csaki, "The Minimal supersymmetric standard model (MSSM)," *Mod.Phys.Lett.*, vol. A11, p. 599, 1996.

[21] Y. Cui, T. Gherghetta, and J. D. Wells, "Emergent Electroweak Symmetry Breaking with Composite W, Z Bosons," *JHEP*, vol. 0911, p. 080, 2009.

[22] H. Terrier, "Overview of LHCb," 2005.

[23] P. Antonioli, "Status of the ALICE experiment at the LHC," 2010.

[24] S. Chatrchyan *et al.*, "Performance of CMS muon reconstruction in pp collision events at $\sqrt{s} = 7$ TeV," *JINST*, vol. 7, p. P10002, 2012.

[25] "Photon reconstruction and identification at sqrt(s) = 7 tev," Tech. Rep. CMS-PAS-EGM-10-005, CERN, 2010. Geneva, 2010.

[26] J. Alwall, M. Herquet, F. Maltoni, O. Mattelaer, and T. Stelzer, "MadGraph 5 : Going Beyond," *JHEP*, vol. 1106, p. 128, 2011.

[27] J. Campbell and R. K. Ellis, "MCFM - Monte Carlo for FeMtobarn processes." http://mcfm.fnal.gov/. Browsed on 2013-05-09.

[28] T. Gleisberg, S. Hoeche, F. Krauss, M. Schonherr, S. Schumann, *et al.*, "Event generation with SHERPA 1.1," *JHEP*, vol. 0902, p. 007, 2009.

[29] T. C. collaboration, "Performance of cms muon reconstruction in pp collision events at s = 7 tev," *Journal of Instrumentation*, vol. 7, no. 10, p. P10002, 2012.

[30] S.Chatrchyan, *et al.*, "Measurement of $w\gamma$ and $z\gamma$ production in pp collisions at $\sqrt{s} =$ 7 tev," *Phys. Lett. B*, vol. 701, p. 535, 2011.

[31] "Absolute calibration of the luminosity measurement at cms: Winter 2012 update," Tech. Rep. CMS-PAS-SMP-12-008, CERN, Geneva, 2012.

[32] S. Kretzer, H. Lai, F. Olness, and W. Tung, "Cteq6 parton distributions with heavy quark mass effects," *Phys.Rev.*, vol. D69, p. 114005, 2004.

[33] T. Sjostrand, S. Mrenna, and P. Z. Skands, "PYTHIA 6.4 Physics and Manual," *JHEP*, vol. 0605, p. 026, 2006.

[34] G. Cowan, K. Cranmer, E. Gross, O. Vitells, "Asymptotic formulae for likelihood-based tests of new physics," *Eur.Phys.J.*, vol. C71, p. 1554, 2011.

[35] U. Baur, T. Han, and J. Ohnemus, "QCD corrections and anomalous couplings in $Z\gamma$ production at hadron colliders," *Phys.Rev.*, vol. D57, pp. 2823–2836, 1998.